POLITECNICO DI TORINO

Master’s Degree in Energy and Nuclear Engineering

Master’s Degree Thesis

3D Printing of BZY and BZCY Electrolytes for Protonic Ceramic Electrolysis Cells

Supervisors
Prof. Federico Smeacetto
Dr. Simone Anelli

Candidate
Turkan Utku Tezsezer

Academic Year 2024/2025

Bana ve hayallerime yürekten inanan, attığım her adımda yanımda olan ve bana sonsuz destek veren sevgili anne ve babama…

To my parents and friends who always supported me and believed in me…

Abstract

Due to the negative impact of traditional energy resources on the atmosphere, there is a growing shift toward sustainable alternatives. Hydrogen has emerged as a key player as energy vector in reducing greenhouse gas emissions and storing renewable energy. In recent years, producing green hydrogen through water electrolysis with reversible electrochemical devices has become a viable solution. Among hydrogen production methods, protonic ceramic electrolysis cells (PCECs) are gaining attention for their high efficiency, adaptability, and performance at lower operating temperatures (400–700°C). Despite these advantages, challenges remain in optimizing materials and manufacturing methods to improve PCEC performance, scalability and durability.

This study focuses on innovative approaches to manufacturing PCEC electrolytes using additive manufacturing (AM) techniques to enhance reliability, precision, and performance. Two AM techniques, 3D-Digital Light Processing (DLP) and Robocasting (RC), were applied to fabricate the PCEC electrolyte. Custom-formulated photocurable and robocasting slurries were developed and analysed for rheological properties, polymerization behaviour, and structural integrity. Heating stage microscopy (HSM) was used to study thermal behaviour during processing, while SEM-EDX characterization provided insights into microstructural properties. These findings contribute to advancing PCEC manufacturing, offering a pathway to adjustable, efficient, and durable energy devices for a sustainable future

Contents

List of Figures

Chapter I

Chapter II

Chapter III

List of Tables

Chapter I

Chapter II

Chapter III

List of Acronyms

PCEC	Protonic Ceramic Electrolysis Cell
AM	Additive Manufacturing
DLP	Digital Light Processing
RC	Robocasting
PEMEC	Proton Exchange Membrane Electrolysis Cell
AEC	Alkaline Electrolysis Cell
MSEC	Molten Salt Electrolysis Cell
SOEC	Solid Oxide Electrolysis Cell
AEM	Anion Exchange Membrane
PCFC	Protonic Ceramic Fuel Cell
VP	Vat-Photopolymerization
SLA	Stereolithography
RI	Refractive Index
BZY	Barium yttrium zirconate
BZCY	Barium cerium yttrium zirconate
YSZ	Yttria-Stabilized Zirconia
CTE	Coefficient of Thermal Expansion
HSM	Heating Stage Microscopy
EDX	Energy Dispersive X-Ray spectroscopy
SEM	Scanning Electron Microscopy
XRD	X-ray Diffraction

UV-visible	Ultraviolet-visible spectroscopy
BAPO	Phenylbis(2,4,6-trimethylbenzoyl) phosphineoxide
TMPTA	Trimethylolpropane triacrylate
PEGDA250	Poly (ethylene glycol) diacrylate
HDDA	1,6-Hexanediol diacrylate

CHAPTER I

Introduction

1.1 The role of Hydrogen in Clean Energy Transition

As the global population increases the necessity for energy increases as well. There are other factors affecting this situation such as increase in consumption rate and the developments in technology over the years. The current energy resources: such as fossil fuels, natural gas, oil still plays a big role in the energy sector, however these resources will not provide for the energy demand forever. Moreover, the fossil fuels also have a negative impact on the environment and human health. These impacts caused people to search for environment friendly solutions such as renewable resources, wind, solar power; due to their intermittent nature they require clean energy vectors, such as hydrogen.

Due to fossil fuel consumption, the emissions of greenhouse gases (CO_2, CO, CH_4) in the atmosphere have increased rapidly over the years, resulting in a rise in Earth's temperature. To mitigate these effects, the goal is to reduce carbon emissions to the minimum level of residual emissions, known as net zero. Net zero aims to reach a Carbon neutrality by 2050 by limiting the global temperature increment to 1.5 °C (1).

According to IRENA, in the 1.5°C Scenario, clean hydrogen and its derivatives account for 12% of the overall reduction in carbon dioxide (CO_2) emissions by 2050. For achieving this goal, the clean hydrogen production needs to increase from 0.7 million tonnes in 2022 to 523 million tonnes annually by 2050. The share of green hydrogen in clean hydrogen is expected to be 94% in 2050 (2). Hydrogen is a clean and efficient energy vector that can be produced from many different sources.

Hydrogen can be categorized in three groups: grey, blue and green hydrogen. Grey hydrogen is produced from fossil fuels through gasification or reforming, blue hydrogen also comes from fossil fuels following a similar path the with the only difference that, it can be produced from also carbon capture. Green hydrogen is produced directly from renewable energies and its utilization is free of toxic gas formation as well as CO_2 emission (3).

Hydrogen has the ability to provide great amount of energy per mass due to its high weight specific energy density (33 kWh/kg), which is even higher than that of gasoline's (12.2 kWh/kg). Furthermore, hydrogen can be stored in high pressure cylinders or in a liquid state by using cryogenic tanks. However, its low density presents a major limitation to storage. (4). Hydrogen can be produced in various ways (through electrolysis from renewable electricity, through carbon capture) to be used in different industries such as in transportation, heating and power generation. It is also possible to produce synthetic fuels by combining CO_2 with hydrogen through carbon capture. (Figure 1.1).

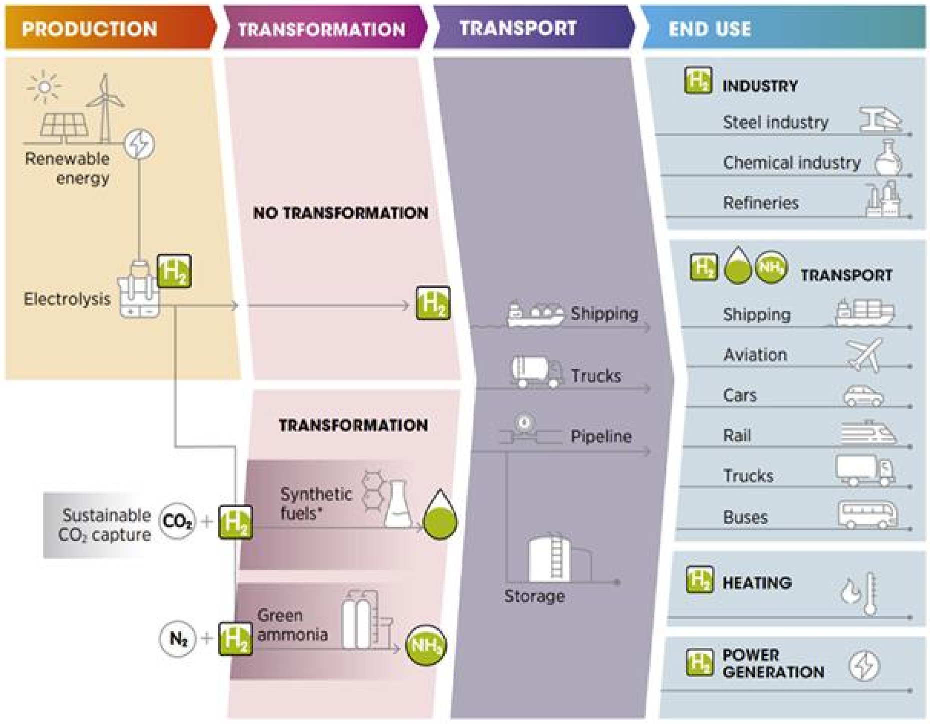

Source: IRENA

* The term synthetic fuels refers here to a range of hydrogen-based fuels produced through chemical processes with a carbon source (CO and CO_2 captured from emission streams, biogenic sources or directly from the air). They include methanol, jet fuels, methane and other hydrocarbons. The main advantage of these fuels is that they can be used to replace their fossil fuel-based counterparts and in many cases be used as direct replacements – that is, as drop-in fuels. Synthetic fuels produce carbon emissions when combusted, but if their production process consumes the same amount of CO_2, in principle it allows them to have net-zero carbon emissions.

Figure 1. 1 Green Hydrogen production, transformation, transport and end use (IRENA) (3)

Hydrogen can be used in various applications as a feedstock, reducing agent, or fuel. Burning hydrogen can generate heat exceeding 1,000°C without producing any CO_2 emissions. Moreover, hydrogen can also be used in fuel cells to chemically react with oxygen to produce electricity without emitting pollutants or greenhouse gases. The only byproduct produced is water vapor. (3).

Nowadays hydrogen gas is mostly used in the petrochemical industry as a feedstock and in the steel industry as a reducing agent. There are several factors effecting green hydrogen's full contribution to the industrial sector such as the lack of competition with fossil fuels, cost, end use technologies being not fully developed. According to IRENA, policy regulations play a crucial role in this, policy makers can adopt industrial policies that address these problems and oblige or support a change from fossil fuel dependency in hard-to-abate sectors (3).

The latest findings show that in 2022 the global hydrogen production reached almost 95 Mt, which is 3% greater than 2021. But a big portion of the production comes from Natural gas as a by- product, which corresponds to grey hydrogen. The hydrogen produced from water electrolysis is around 0.1% of today's global hydrogen production. Even though the share of green hydrogen in global production is small the installed capacity and the number of projects are increasing rapidly. By the end of 2022, the global installed water electrolyser capacity for hydrogen production had reached almost 700 MW, a 20% increase compared to the previous year (5).

1.2 Electrolysis and Types of Electrolysis Cells

An electrolysis cells, is a device where the chemical reactions take place using electricity. It is formed by two electrodes: an anode where the oxidation reaction takes place, and a cathode where a reduction reaction occurs. These two electrodes are separated by an electrolyte. Electrical energy enters the cells from an external circuit and starts the chemical reactions that result in gaseous products.

One way to produce hydrogen can be through an electrochemical water splitting technique also known as water electrolysis. The basic reaction for water electrolysis is shown in Eq. (1.1).

$$H_2O + Electricity\ (237.2\ KJmol^{-1}) + Heat(48.6\ KJmol^{-1}) \rightarrow H_2 + \frac{1}{2}O_2 \qquad (1.1)$$

Table 1.1 shows the main water electrolysis technologies indicating the developments status and information about the flexibility, operating conditions, cost. Alkaline and PEM electrolysers are well established technology while SOEC is still under demonstration and AEM is under research.

Table 1.1 Main water electrolysis technologies (IRENA) (3)

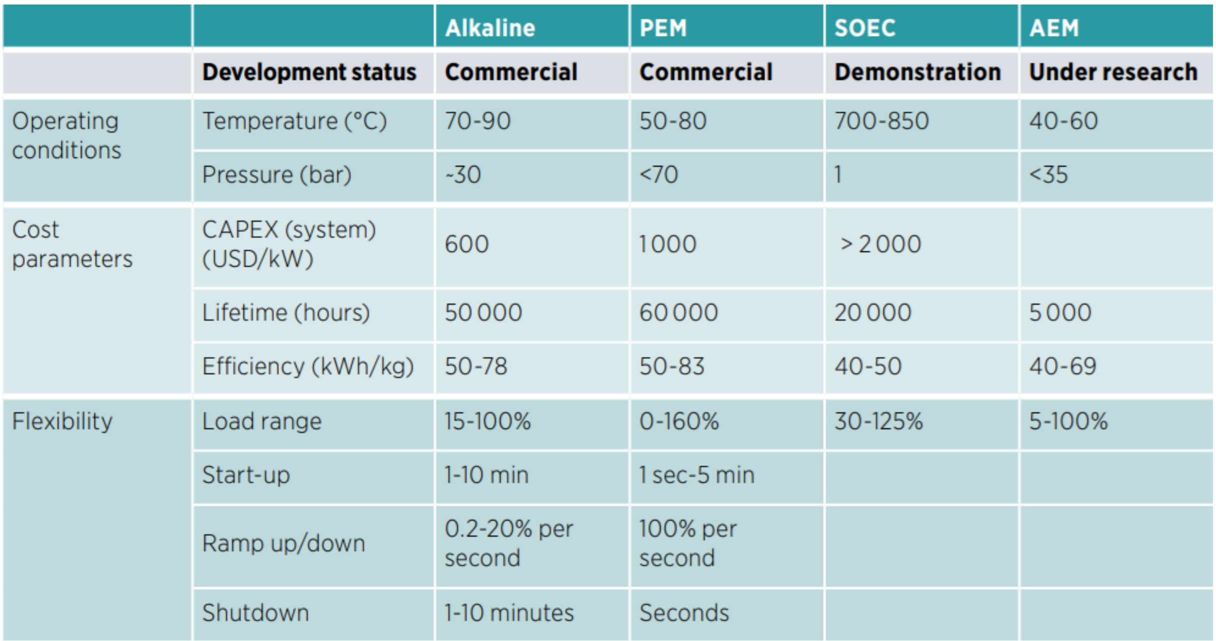

		Alkaline	**PEM**	**SOEC**	**AEM**
	Development status	**Commercial**	**Commercial**	**Demonstration**	**Under research**
Operating conditions	Temperature (°C)	70-90	50-80	700-850	40-60
	Pressure (bar)	~30	<70	1	<35
Cost parameters	CAPEX (system) (USD/kW)	600	1000	> 2000	
	Lifetime (hours)	50 000	60 000	20 000	5 000
	Efficiency (kWh/kg)	50-78	50-83	40-50	40-69
Flexibility	Load range	15-100%	0-160%	30-125%	5-100%
	Start-up	1-10 min	1 sec-5 min		
	Ramp up/down	0.2-20% per second	100% per second		
	Shutdown	1-10 minutes	Seconds		

Since the 18th century, the development of water electrolysis technologies has continued and been used in industrial applications (6). Water electrolysis has been a popular method for producing green hydrogen over the past two centuries. However, due to economic challenges, only 4% of hydrogen (65 million tons) is produced via water electrolysis.

Throughout these developments four different types of electrolysers were introduced: proton exchange membrane electrolysis cells (PEMEC), alkaline electrolysis cells (AECs), molten salt electrolysis cells (MSEC) and solid oxide electrolysis cells (SOECs).

In PEMEC the water is split electrochemically into hydrogen and oxygen, at the anode side the water is split into oxygen (O_2), protons (H^+) and electrons (e^-). The protons travel through the proton conducting membrane to the cathode side and the electrons moves from the anode side through the external power circuit, that provides electric energy to the cell.

In AECs, the water is split into hydrogen and OH^-at the cathode, OH^- is the charge carrier that flows through the electrolyte to the anode side where the oxygen and water is produced. In AECs, asbestos diaphragm and nickel materials are used as the electrodes. The diaphragm separates the gases that are produced during the electrolysis process. Alkaline electrolysis has negative sides such as the fact that current densities are limited, the operating pressure is low so does the energy efficiency. A new approach for alkaline electrolysis is under development, the idea is to replace the asbestos diaphragm with anion exchange membranes (AEM) made of polymers with anionic conductivity (7).

SOEC is very popular due its ability to produce hydrogen with high efficiency while converting electrical energy to chemical energy. It operates at high temperatures and pressure (500-900°C) while processing conventionally. It uses O_2 conductors which are mostly made of nickel/yttria stabilized zirconia (8). However, instability and degradation are the main problems, which creates a barrier towards commercialization.

Currently, developments and studies on the use of ceramic proton-conducting materials in electrolysis cells are ongoing. These materials show high ionic conductivity and they are efficient with an operating temperature range of 400-700 °C.

MSEC uses molten carbonates as the electrolyte due to their high ionic conductivity and low cost. These types of electrolysers are mainly used for the carbon dioxide reduction, i.e. $CO_2$is reduced to solid carbonaceous species such as carbon spheres, carbon nanotubes, and carbon flakes on the surface of the cathode. This makes the reaction discontinuous due to the frequent replacement of the cathode (9).

Generally, both the electrolysers and fuel cells are classified according to the operating temperatures and electrolyte materials. Table 1.2 shows the type of materials that are used in different water electrolysis technologies.

Table 2.2 Materials used for water electrolysis technologies (IRENA) (10)

	Alkaline	**AEM**	**PEM**	**Solid Oxide**
Electrolyte	KOH/NaOH	DVB polymer support with 1 M KOH/NaOH	Solid polymer electrolyte (PFSA)	Yttria stabilized Zirconia (YSZ)
Separator	Asbestos/Zirfon/Ni	Fumatech	Nafion	Solid electrolyte YSZ
Electrode/Catalyst (Hydrogen side)	Nickel coated perforated stainless steel	Nickel	Iridium oxide	Ni/YSZ
Electrode/Catalyst (Oxygen side)	Nickel coated perforated stainless steel	Nickel or NiFeCo alloys	Platinum carbon	Perovskites (LSCF, LSM) (La,Sr,Co,FE) (La,Sr,Mn)
Gas Diffusion layer	Nickel mesh	Nickel foam/carbon cloth	Titanium mesh/carbon cloth	Nickel mesh/foam
Bipolar Plates	Stainless steel/Nickel coated stainless steel	Stainless steel/Nickel coated stainless steel	Platinum/Gold-coated Titanium or Titanium	Cobalt coated stainless steel

1.3 Protonic Ceramic Electrolysis Cells (PCECs)

PCECs are a promising technology due to their capability of combining high efficiency and flexibility under varied working conditions. They have many advantages over the SOECs, in PCECs it is possible to operate at lower operation temperatures. Additionally, unlike SOECs, which produce undiluted oxygen that requires regulation to avoid safety hazards and cell degradation, PCECs present no such risk due to the absence of undiluted oxygen.

The main difference between the SOECs and PCECs are the charge carrier that is transferred over the electrolyte. In PCECs when an external voltage is applied to the cell, protons are flowing through the electrolyte instead of oxide ions. The working mechanism is based on the electrochemical splitting of steam, which is fed to the anode and broken down into protons and oxygen.

Afterwards, the protons move through the dense electrolyte layer, electrolyte layer must be dense to avoid mixing of oxygen ions or molecular gasses to the cathode. Later, these protons combine with electrons to form the pure and dry H_2 steam.

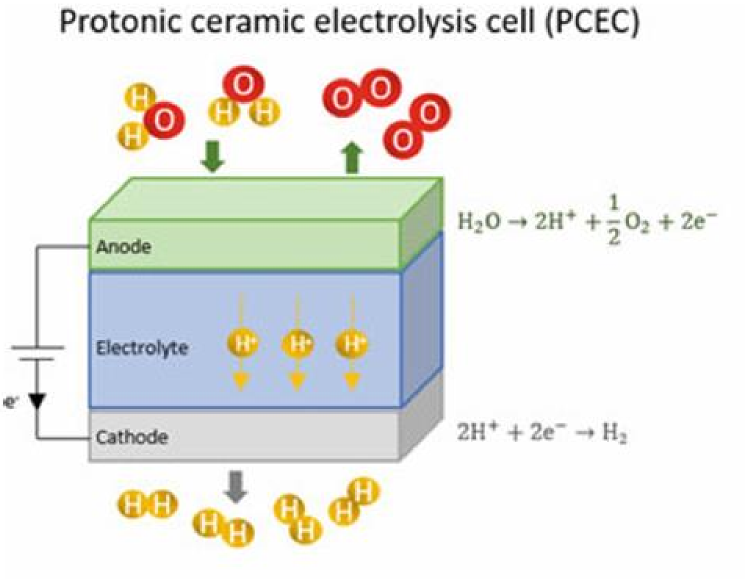

Figure 1. 2 Protonic ceramic electrolysis cell working mechanism (PCEC) (11)

In SOECs the working mechanism is the opposite of PCECs. Dry steam needs to be fed to the fuel electrode, steam molecules follow a reduction reaction and as a result H_2 is collected in the fuel electrode chamber. Oxygen ions migrate to the air electrode by passing through the dense electrolyte, it follows an oxidation reaction which forms a high-purity oxygen gas steam.

As can be seen from Figure 1.2 PCEC contains three layers that have different purposes. 1) a dense protonic ceramic electrolyte, 2) a porous air electrode where the oxygen evolution reaction (OER) occurs and 3) a porous fuel electrode where the hydrogen evolution reaction (HER) occurs (11) .

The following characteristics of the three main components are:

- Protonic electrolyte: the material should have high protonic conductivity with negligible electronic conductivity under operation conditions. It should be dense to avoid gas permeability.
- Air electrode (anode in electrolysis mode): the materials need to have high electronic conductivity for current collection and high ionic (protonic and oxygen ion) conductivity in addition to electrocatalytic activity. The electrode should possess an optimized microstructure allowing the diffusion of steam and O_2removal.
- Hydrogen/fuel electrode (cathode in electrolysis mode): the component, usually a composite material, should present high electronic and protonic conductivity. Nowadays, most of the cathodes are based on Ni-based composite materials (11).

Dry and pure compressed H_2,is obtained as a final product in the protonic electrolyser by regulating the operating pressure on the fuel electrode and the operation current density. This technology is more cost-efficient and reduces system complexity (11).

Theoretical analysis also showed that the reversible operating mode would be more favourable with proton conducting cells in terms of energy conversion efficiency. The whole device is well-known as reversible protonic ceramic electrochemical cell. In the case of an electricity surplus the cell can act as an electrolyser and if there is a demand for electricity it can act on the fuel cell mode. Protonic ceramic fuel cells generate electricity by exploiting the chemical energy of the reactants. The process starts by sending the hydrogen to the fuel electrode, where the reduction reaction takes places and protons are generated (Eq 1.2).

$$H_2 \rightarrow 2H^+ + 2e^- \qquad \text{(Eq 1.2)}$$

The protons pass through the electrolyte and the electrons flow through the external circuit, supplying a load. A mass flow rate of air is sent to the oxygen electrode side. Once the protons and the electrons reach the oxygen electrode, they react to form water (Eq. 1.3).

$$\frac{1}{2}O_2 + 2H^+ + 2e^- \rightarrow H_2O \qquad \text{(Eq 1.3)}$$

The formation of water on the oxygen electrode side is a very huge advantage because it prevents the dilution of fuel at the anode and enhances the reusability of unreacted hydrogen fuel (12). Regardless of the advantages, there are still many challenges which needs to be overcome to promote the use of PCECs.

Over the last decades protonic ceramic electrochemical cells (PCECs) draw less attention compared to solid oxide cells (SOCs) due to the complexity of the fabrication of the device, which includes; 1) poor electrolyte sinterability or low chemical stability, 2) lack of reliable and cost-effective manufacturing routes or 3) large overpotentials of the electrodes, involving poor activity of the steam electrode for the water splitting reaction (12).

1.4 Protonic Ceramic Electrolysis Cell Materials

1.4.1 Protonic Electrolyte Materials

The electrolyte layer positions in between two different environments, steam electrode and hydrogen electrode, and it acts as the ionic permeable membrane. It is also joined with the other components of the cell to create the structure. The electrolytes need to exhibit the following requirements;

- Non- permeability: the electrolyte needs to have minimal porosity to avoid the mixing of gasses that are produced in anode and cathode.
- It needs to be dense: ceramic electrolyte needs to be sintered to avoid undesirable facilitated migration of cations from one phase to another.
- High ionic conductivity: the energy conversion process is based on the electrochemical properties of the electrolytes. In both fuel cells and electrolysis cells, which are regulated by the ohmic resistance contribution, it can be minimized by reducing the thickness of the electrolyte or by using highly conductive cells.
- Low electronic conductivity: in the case of electric conductivity, the electric current flows through the electrolyte and causes short circuit, leading to efficiency reduction.

- Good thermomechanical compatibility with the different materials of the cell: As mentioned before the cell is composed of different layers and in each layer, different materials are used. The electrolyte needs to have good thermomechanical compatibility with the joining materials. (12), (13)

When analysing the challenges and possible solutions regarding the protonic ceramic electrolyte materials, the main focus is on the barium cerate ($BaCeO_3$) and barium zirconate ($BaZrO_3$) families. This is due to their good protonic conductivity as they increase the proton conductivity by introducing more oxygen vacancies. Electrical performance tests have been conducted on the doped cerates and zirconate- based proton conductors. It is observed that, cerate- based perovskites show higher proton conductivity (10^{-2} to 10^{-1} S cm^{-1} at 600°C) than that of zirconate- based perovskites (~10^{-3} S cm^{-1} at 600°C) (14) .

In terms of chemical stability and mechanical strength, zirconate-based ceramics show better behaviour, since cerate-based ceramics show chemically unstable behaviour in CO_2 and H_2O containing atmospheres at typical operation conditions. On the other hand, $BaZrO_3$ – based oxides need high sintering temperatures resulting in manufacturing challenges and small grained microstructure. This results in low proton conductivity and a high-density of grain boundaries (13).

In the case of $BaCeO_3$-based electrolytes the goal is to improve their stability, co- doping strategy plays an important role in this. In co- doping strategy, different type of ions is introduced for the optimization of the electrical properties.

There are other types of proton conducting simple oxides such as fluorite type and the phosphate type. The proton conductivity is affected by the material properties such as crystal structure and microstructure. In the case of simple oxide systems, such as yttria-stabilized zirconia (YSZ): interfacial protonic conductivity is highly dependent on the grain size. The primary source of proton conductivity in these systems is the absorbed water at the grain boundary interphases, enhancing the conductivity.

In phosphate type, the conductivity increases with temperature and the wet atmosphere, the water molecules interact with phosphate groups forming a network that increases the proton mobility (15).

Figure 1.3 indicates the conductivity of various electrolyte materials for SOEC and PCEC at different temperature levels. It is evident that BZY, BZCY721 and BCZYYb shows higher ionic conductivity at the intermediate temperature range compared to the typical SoA electrolytes for SOEC, e.g., YSZ and GDC. This is due to the lower activation energy exhibited by proton-conducting perovskites, since smaller size of carrier species results in a lower activation energy for the conduction process (16).

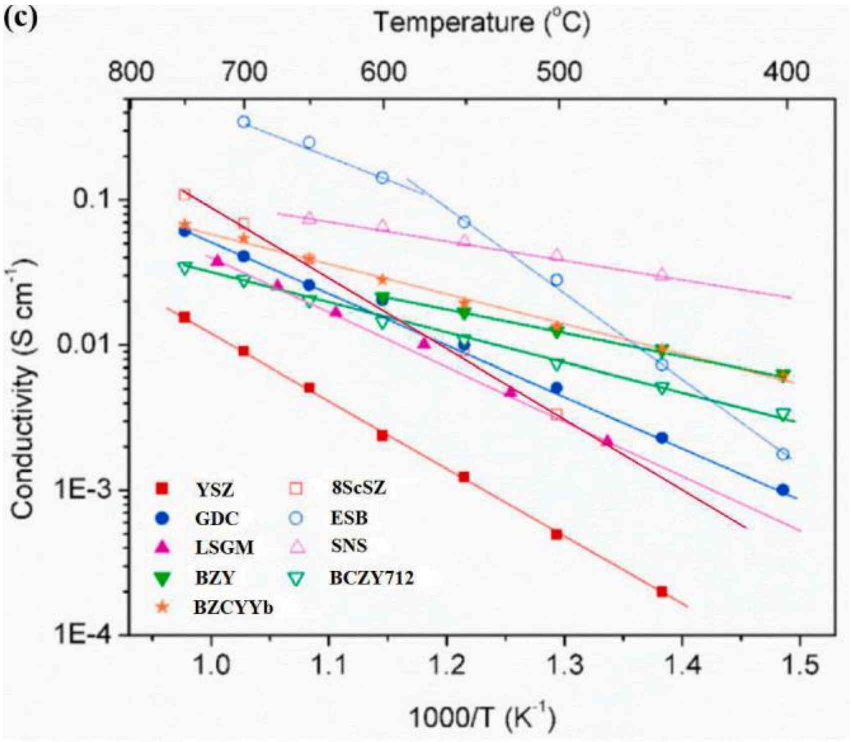

Figure 1. 3 Comparison of ionic conductivity of various proton conductive electrolytes and oxygen ions conductive electrolytes (17)

1.4.2 Electrode Materials

The electrode materials used in the PCECs are neither purely ionic nor electronic conductors and the transport number of the species depends on the operation conditions; i.e., temperature, atmosphere, overpotential and current density applied (11). The main problem about the development of electrodes for PCECs is that there are few materials that can have an appropriate mixture of protonic and electronic conductivity.

Researches are focused on developing different cell configurations to perform electrolysis and reach high efficiency values. Electrodes should fulfil the following requirements in order to reduce the electrodes' overpotential and obtain low polarization resistances (11);

- Stability: electrodes need to be chemically stable during the operation conditions and along the fabrication process.
- Conductivity: they need to have high electronic and ionic conductivity.
- Porosity: unlike the electrolyte layer, the electrodes should have at least 30% porosity. Pores allow fast gas diffusion.
- Coefficient of thermal expansion (CTE) value: the electrodes need to match the CTE values of the electrolyte and the other components of the cell to have good joining.
- Compatibility: electrodes need to be compatible with the rest of the cell components during the operation and fabrication conditions.
- Catalytic activity: electrodes must have sufficient catalytic activity (low polarization resistance) for the redox reactions (11).

1.4.3 Air Electrodes Materials

PCECs use the same strategy as the SOECs; i.e. their air electrode is composed of a composite material. In the air electrode, complex reactions take place such as water splitting, oxygen gas conversion and bulk diffusion which results in higher polarization resistance. The composite material consists of purely electronic conductors and materials with mixed ionic and electronic conductivity. Alternatively, mixed proton and electron-conducting materials can also be used.

The performance of the composite depends on the ratio of the components. Double perovskites are an excellent choice for steam electrode in PCECs due to their structural and compositional flexibility and high electrical conductivity. Among all double perovskites, BaGd0.8La0.2Co2O6-δ (BGLC82) shows the lowest polarization resistance because of its crystal structure capability to incorporate charge carriers in humid environments. (11). One of the problems of these co-containing perovskites is the mismatch in CTE with the electrolyte. In order to solve this problem, composite electrodes have been fabricated.

1.4.4 Fuel Electrodes Materials

In the fuel electrode, the specific surface area plays an important role. The active areas must be enlarged along the electrode. With respect to this, selecting a pure electronic conductor as the fuel electrode is not the best option; because it limits the reaction sites to the electrode/electrolyte surface.

The fuel electrodes are composed of composite materials; the cermet of nickel with a proton conducting electrolyte is predominantly used, particularly the NiO-BCZYYb and NiO-BCZY. This is because the metallic nickel provides excellent catalytic activity for both oxidation and reduction reactions. Additionally, nickel enables an electronic percolation path that ensures efficient electron flow throughout the electrode, which is essential for the cell's overall performance (12), (18), (19).

The fuel electrode of the PCCs has two main advantages over the ones that are used in the SOCs. The first advantage is that the fuel electrode is less influenced by the degree of porosity because the steam production and consumption occur on the air electrode. Secondly, when hydrocarbon fuels are used, the cermet electrode demonstrates high resistance to sulfur and coking. This is due to the high-water uptake properties of proton-conducting materials like BCZY, BCZYYb, and BZY. The absorbed water reacts with the carbon and sulfur on the nickel surface, producing carbon monoxide (CO) and sulfur dioxide (SO_2), thus preventing electrode poisoning (20).

1.4.5 PCC Stack

A stack of cells is an assembly of multiple repeating units of PCEC cells. Each unit consists of a metallic interconnect, a complete PCEC cell (fuel electrode, electrolyte, air electrode), and another metallic interconnect. To separate the two atmospheres, a sealant is placed between the electrolyte and one side of the metallic interconnect.

These interconnects show a direct contact with the anode and the cathode layers. The interconnects provide electrical connectivity between the MEA and the electric load, and enable controlled flow of fuel and oxidizer reactants to the electrodes. A thick anode support (top) and a thin cathode (bottom) sandwich a thin, proton-conducting electrolyte (21).

As can be seen from the Figure 1.4, there are two types of stack configurations, i.e. planar stack and tubular cell configuration. Planar cell configuration is the most extended geometry because it’s easier to be designed and manufactured. For joining purposes, a sealant is used between the interconnect and the electrodes. The sealant also acts as a barrier to prevent contact between the reactants in the electrodes.

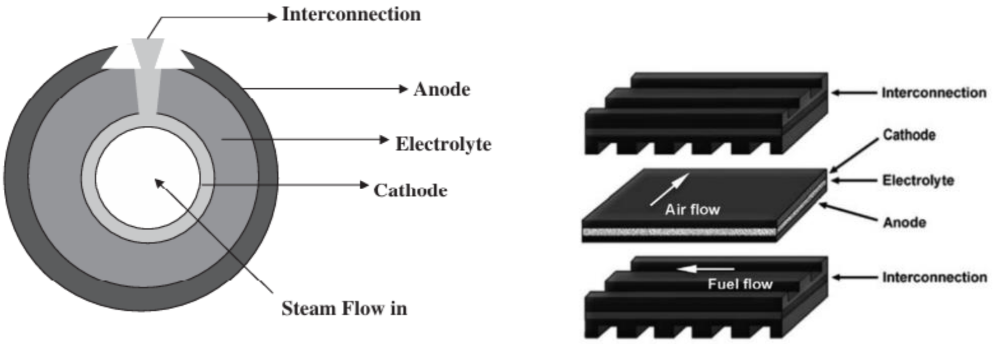

Figure 1. 4 Tubular and Planar configurations of the stack (21)

In the case of Protonic Ceramic Fuel Cells (PCFC) the output voltage and current produced from one cell stack is quite low. For this reason, the cells are connected in series to reach higher voltage values, which results in higher power production. The structures for both fuel cell mode and electrolysis mode are the same with the only difference being that the electrolyte operates in reverse mode in fuel cells. In PCFCs, the water vapor is supplied to the anode and the pure hydrogen is obtained on the cathode side.

1.4.6 Interconnectors

Interconnector plays a crucial role in the PCECs. As mentioned before, since the power generated from one stack cell is not enough usually many stack cells come together to form the device and the interconnect links one stack cell to the neighbouring one. It provides electrical connection between the anode of the cell to the cathode of the neighbouring cell.

The interconnect consists of multiple channels responsible for the flow of reactants and products reaching or exiting the electrodes. Additionally, these channels also act as a barrier, preventing the mixing of chemical species and eliminating the possibility of undesirable chemical reactions.

The interconnect is designed to fulfil different tasks for the better operation of the cell. The interconnect materials need to exhibit the following requirements;

- The interconnect needs to have good electric conductivity and low ionic conductivity, in this way only the electrons can pass through.
- It needs to have adequate stability in terms of chemistry and microstructure.
- Low permeability values are required to prevent the mixing of gases.
- The coefficient of thermal expansion value (CTE) needs to be compatible with other elements of the cell.
- The interconnect should have good thermal conductivity to obtain a uniform temperature in the stack.

When choosing the interconnect material for PCECs, the material's compatibility with the operating environments and temperature is important. Since the PCECs operate at lower temperatures compared to SOECs (approximately 600-800 °C), the interconnect material differs. In PCECs ferritic stainless-steel alloys are a pretty popular choice as an interconnect material. In both PCECs and PCFCs one side of the interconnect is exposed to high steam content in an oxidizing environment and this may result in the degradation of interconnect at intermediate temperatures (22).

Ferritic stainless-steel has low manufacturing cost, suitable oxidation rate and has close thermal expansion value to match with PCEC and PCFC components. They also show high electrical and thermal conductivities. So far, no oxidation study has evaluated a PCFC/PCEC interconnect in both an intermediate temperature range and a higher humidity oxidizing environment (22).

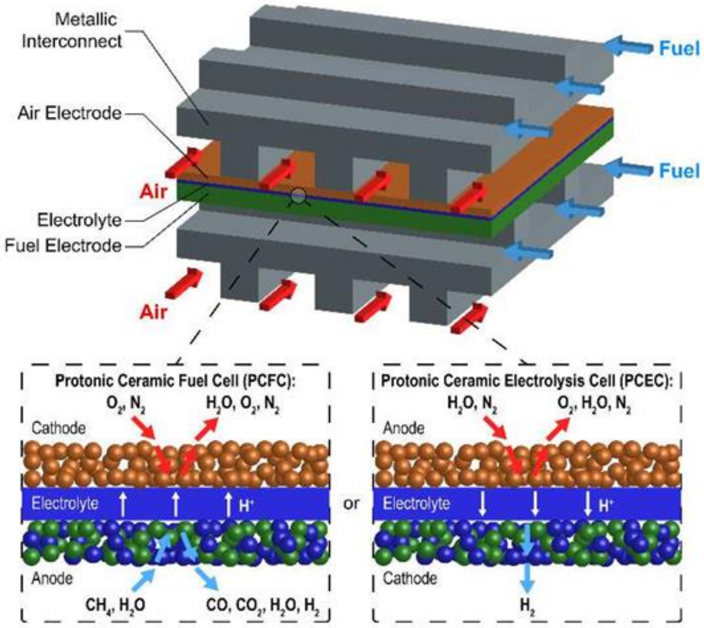

Figure 1. 5 Scheme of the PCFC and PCEC operation in the stack (22)

1.5 Vat-photopolymerization and 3D vat printing

3D vat printing (VP) has gained popularity among researchers as one of the potential methods for fabricating ceramic components. VP offers the ability to print ceramic parts with complex shapes while reducing material usage. Vat photopolymerization is an additive manufacturing technique in which the 3D object is created through a layer-by-layer process, where the photosensitive resin is polymerized by UV light.

Depending on the variation of the curing source the VP process can be classified into: stereolithography (SLA), digital light processing (DLP), two-photon polymerization (2PP), and volumetric 3D printing (23).

SLA photopolymer resins mainly made of monomers, oligomers/ binders, photo-initiators, and some additives. Monomers and oligomers are the main components in the photopolymer resin which forms the crosslinked polymer network. The photopolymer has to be cross-linked, this type of polymer structure shows less creep and higher strength and they also do not melt.

Photo-initiators are responsible from the conversion of the physical energy from the UV light to chemical energy in the form of reactive intermediates. The requirements are for the photo initiator is to have strong absorption of the UV emission wavelength and to undergo a fast photolysis. Photo-initiators react with oligomers and monomers in this way they provide crosslinking to produce polymer chains on exposure to curing light.

DLP generates a rapid entire layer polymerization using digital micro-mirrors devices while SLA uses a laser coming from a single point which is reflected by the scanning mirror. For this reason, DLP provides a higher printing speed and better distribution than SLA (23). Figure 1.6 shows the SLA and DLP working processes.

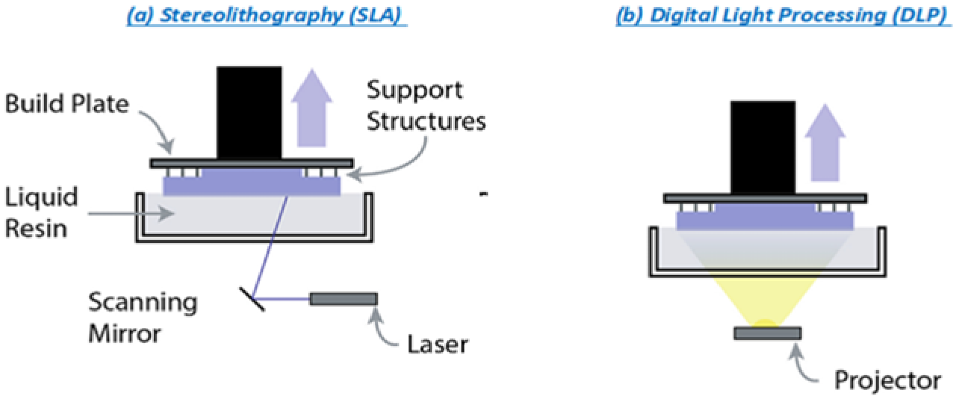

Figure 1. 6 Working principles of SLA and DLP (23)

Producing ceramic parts using this technique requires a slurry in which ceramic powder and photo-active resin are mixed. During the process, the ceramic powders trapped within the cross-linked polymer network are cured by UV light, followed by de-binding and sintering. The aim is to achieve a uniform microstructure of the 3D printed ceramics.

1.6 Goal of the Thesis

The goal of the thesis is to manufacture the electrolyte of the PCECs by using two additive manufacturing (AM) techniques, vat-photopolymerization DLP and Robocasting (RC).

Photocurable pastes for DLP and thermo-curable, solvent-based pastes for Robocasting have been formulated. The rheology of both types of pastes has been analysed. Additionally, for the DLP pastes, polymerization has been analysed. Moreover, ultraviolet-visible spectroscopy (UV-visible) analyses of the paste have been conducted to determine the feasibility of the process.

After these analyses are completed, the electrolyte for the PCECs will be fabricated using the DLP and Robocasting techniques. The samples will be studied using heating stage microscopy (HSM). Once the ceramic green body is obtained, it will undergo de-binding and sintering processes to achieve the densified ceramic part.

The microstructure of the sintered printed samples will be examined using scanning electron microscopy (SEM) combined with energy-dispersive X-ray spectroscopy (EDX). The results obtained from these analyses will be discussed in Chapter III, focusing on the steps taken to improve the stability of the slurries, addressing the problems encountered during the experiments, and the outcomes achieved.

Chapter II

Materials and Methods

2.1 Formulation of Photocurable Slurries for 3D DLP process

Aiming to 3D print BZY structures by DLP different photocurable slurries have been prepared. The slurry that was prepared for this process contains a polymer matrix and ceramic fillers. Stabilization and the homogenization of the slurry plays a crucial role to achieve a uniform microstructure of the printed ceramic. To obtain an homogenic slurry a good dispersion of the particles is required.

Ceramic powders have hydroxyl groups on their surfaces, this makes them hydrophilic and limits the compatibility with resins (24).

The slurry composition is the following: an acrylate-based monomer, a photo-initiator which also shifts the absorption to longer wavelengths and with the monomers it forms the cross-linked polymer network. Surfactants are included in the composition, whose role is to decrease the surface tension and enhance wetting, they improve the interaction between the ceramic particles and the polymer resin. In order to maintain the slurry stability dispersants and plasticizers are used. When dispersant is added to the composition, they are absorbed on the particle surface and form a network between the particles and the monomer. They also affect the rheological behaviour of the ceramic suspension.

Plasticizers regulate the rheological behaviour of the ceramic slurry. By using plasticizers and dispersants together, it is possible to reduce the inter-particle forces to establish high solid loading with low viscosity.

Plasticizers have three roles in manufacturing of ceramics:

- The plasticizer molecule interpolates between the polymers thus increase the space between the polymers and reduce the Van der Waals forces and friction between the particles.
- They can reduce the glass transition temperature of the polymer after the printing, resulting in better flexibility of the green body.
- They can reduce the inner stress of the green body and help the suppression of defects such as cracks (25).

Two ceramic powders were chosen for this application; BZY (Barium Yttrium Zirconate) and BZCY (Barium Cerium Yttrium Zirconate). A slurry is prepared by using BAPO (used as photo-initiator), TMPTA (used as monomer), Disperbyk103 (dispersant) and PEG400 (plasticizer). Multiple slurries were made to obtain the optimal one for the case. In Figure 3.1 and 3.2, the chemical formulation of BAPO and TMPTA and HDDA can be seen.

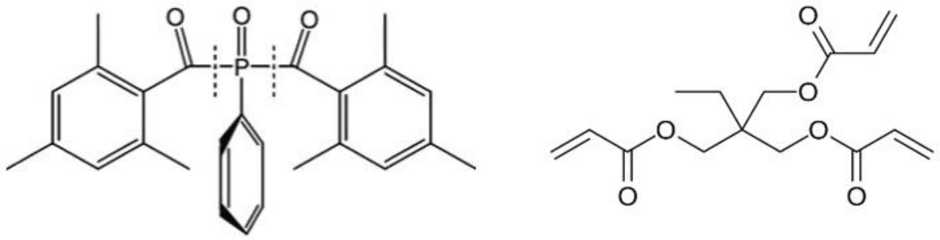

Figure 2. 1 The molecular structure of BAPO and TMPTA (Trimethylolpropane triacrylate)

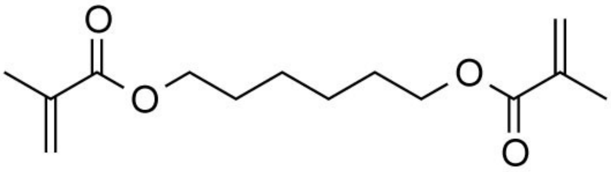

Figure 2. 2 Molecular Structure of HDDA (1,6 hexandiol diacrylate)

The components used in this thesis, for the preparation of the slurries for 3D DLP process are indicated in the table below.

Table 2. 1 Components for DLP slurries

Ceramic Powders Formulation	
BZY	Barium yttrium zirconate
BZCY	Barium cerium yttrium zirconate
Photo-initiator Formulation	
BAPO	Phenylbis(2,4,6-trimethylbenzoyl) phosphineoxide
Monomer Formulation	
TMPTA	Trimethylolpropane triacrylate
PEGDA250	Poly (ethylene glycol) diacrylate
HDDA	1,6-Hexanediol diacrylate
Dispersant Formulation	
Disperbyk103	polyester phosphoric acid ester
Monofax	Mono And Di-Phosphate Esters
Plasticizer Formulation	
PEG400	Polyethylene Glycol 400

In order to obtain a homogenous and stable slurry with a low viscosity, the dispersant concentration needs to be optimized, otherwise agglomeration and flocculation can occur. These situations can affect the printing process and can result in low accuracy in the 3D DLP process.

The ceramic loading of the slurries was calculated to obtain a homogenous and stable slurry, while also the rheological behaviour is taken into account. Several slurries were prepared to determine the optimal formulation. To ensure better homogeneity, the solid load concentration was maintained at a range between 55 wt% to 60 wt%, with the dispersant added at ≈4 wt% relative to the solid load and the photo-initiator set at 1 wt%.

After formulating the composition, the slurry preparation begins. First, the required amount of photo-initiator (BAPO) is carefully weighted in a fume hood using an analytical balance, ensuring accuracy and safety. The same procedure is then repeated for the monomer (TMPTA), conducted at room temperature in a dark environment to prevent any degradation. Following this, the mixture is transferred to a Thinky mixer, where it is blended for 15 minutes at 800 rpm to ensure thorough mixing.

Next, the dispersant and plasticizer are weighed and incorporated into the mixture, which is then stirred for an additional 5 minutes at 1200 rpm. To achieve optimal homogeneity, the ceramic powder is added in four equal stages, with the mixture being blended for 5 minutes after each addition. Finally, a defoaming step is carried out to eliminate any trapped air. The slurry is stored in a bottle, which is wrapped in aluminium foil to protect it from light exposure, ensuring its stability.

2.2 Formulation of Solvent Based Slurries for Robocasting (RC)

Aiming to deposit by robocasting BZCY substrates, several slurries have been prepared. The components of such slurries are: a binder, solvent, dispersant, plasticizer and ceramic powder.

To obtain a homogenous deposition a good dispersion of the soling loading into the solvent is required. Agglomeration and flocculation of the particles can occur during the preparation of the slurry. This might cause destabilization of the slurry can create problems such as the clogging of the nozzles and compromise the quality of the final deposition result.

Various recipes were tried to obtain the optimal one: the solid load concentration was set as ≈65 wt%, the plasticizer amount was 20 wt% and the binder concentration was 5 wt% of the total liquid. The amount of dispersant was 4 wt% with respect to the solid load. The solvent concentration was determined by subtracting all the liquid components from the total volume of the liquid.

The components used in this thesis are indicated in the table below, it also shows the solid loading percentage and the concentrations of the other components that are used in the composition.

Table 2. 2 Components for RC slurries

	Compounds	**Concentration**
BZCY	$(BaCe_{(1-x-y)}Y_{(x)}Zr_{(y)}O_3)$	70-65%wt
Propylene Glycol and Polyvinylpyrrolidone	PG+K90 (10%wt)	5%wt
Propylene Glycol (PG)	CH3CH(OH)CH2OH	6%wt
Polyethylene Glycol 400 (PEG400)	$C_{2n}H_{4n+2}O_{n+1}$	20%wt
Monofax	Mono And Di-Phosphate Esters	4%wt
Disperbyk103	polyester phosphoric acid ester	4%wt

BZCY was selected as the ceramic powder. A solution containing PG and K90 was prepared (with K90 at a 10 wt% concentration in the solution) and used as the binder. Two dispersants, Monofax and Disperbyk103, were chosen and used separately in the slurry. Lastly, PEG400 was selected as the plasticizer.

The preparation of the slurry involves several steps. First, the binder, plasticizer, dispersant, and solvent are accurately weighted under a fume hood using a scale. These components are then combined, and the mixture is blended for 5 minutes at 1200 rpm using a Thinky mixer.

Next, the ceramic load is gradually added in five stages, with the mixture being blended for a specified duration at each step. Following this, a defoaming process is carried out, and the slurry is mixed for an additional 15 minutes at a higher rpm to ensure optimal homogeneity.

2.3 Rheological Analysis

Rheological analysis of the prepared slurries is done by using a H20 Rheometer and the viscosity is measured. Calibration needs to be done before the measurement to obtain reliable results. All the measurements are performed in Politecnico di Torino, DISAT.

Rheometer is a device which measures the viscosity of the viscous fluids (slurry, liquid). It shows the behaviour of the slurry when a force or a velocity is applied. The slurry is in contact with a surface and the measuring is performed through this surface. Some examples of the geometries used for this purpose include tubes, parallel plates, cone-and-plate arrangements, and concentric cylinders. The aim of such viscometry is then,

- To convert the applied force F to a shear stress σ, and
- To convert the velocity V to a shear rate γ. (26)

Geometric constants are used during the measurement and are evaluated at a standard reference point, in addition to temperature (usually ambient temperature is chosen).

Then, the calculated shear stress and shear rate can be plotted as a function of one another. If the shear stress is divided by the shear rate viscosity will be obtained. If the measured viscosity shows a constant behaviour, then the liquid is classified as Newtonian.

The viscosity of a Newtonian liquid does not vary with deformation rate or time. However, in the case of structured liquids such as polymer solutions, the viscosity decreases as the shear rate increases. These liquids are referred to as shear thinning. In such materials, the relationship between viscosity and shear rate is non-linear.

The slurries prepared both for the photopolymerization 3D printing and robocasting need to show non-Newtonian behaviour with a reversible-shear thinning behaviour in order to facilitate the extrusion of the material and to maintain the shape afterwards. For the DLP slurries, the low viscosity values are favourable for the self- levelling behaviour to achieve high accuracy in the printing process.

Additionally, the composition also affects the viscosity behaviour. By adjusting the percentage of dispersants, binders and plasticizers in the slurry, it is possible to observe different viscosity behaviours.

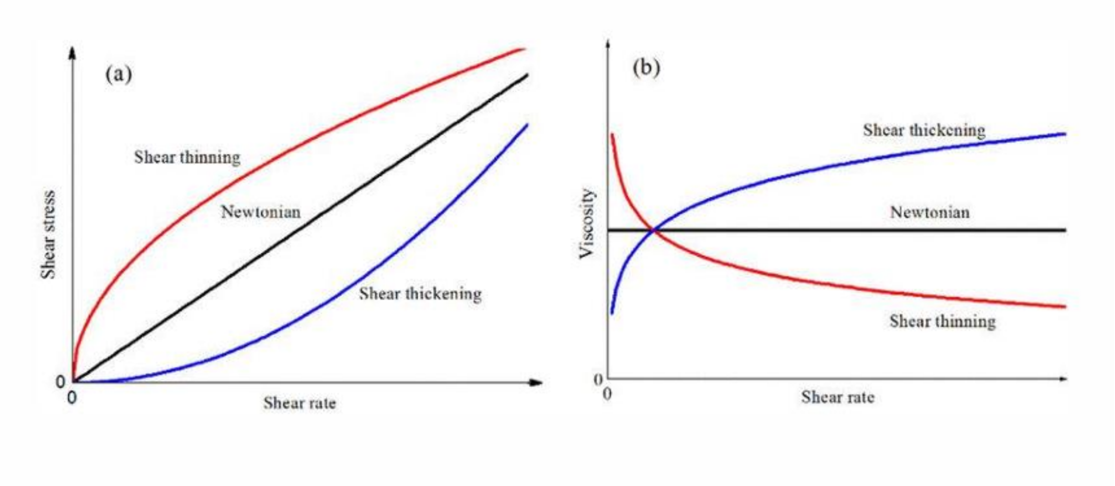

Figure 2. 3 Rheological behaviours depending on the shear rate and shear stress

Figure 2. 4 Rheometer HR20 (Politecnico di Torino, DISAT)

2.4 Polymerization Test and Cure Depth

To observe the curing behaviour of the slurries, polymerization test is conducted by using the ASIGA MAX DLP printer. A small amount of slurry was cured with 19 mW/ cm^2 of light, each sample was exposed to the light source for different duration times. The thickness of the samples was measured by using a micrometer gauge ($C_d, cure\ depth$).

During this process the photo-initiators are activated and create free radicals, which cause the polymerization of the monomers. The polymerization increases until the gel point is reached. The gel point represents the soft solid state. The intensity of the light decreases as it propagates into the depth below the surface ($depth\ z$). The depth at which the gel point occurs is called the cure depth (C_d), at this depth the energy dose is sufficient enough to reach the gel point, and the energy dose is called as the critical energy dose (E_c).

The relationship between the cure depth and the energy dose(E) can be expressed by the Jacob's cure depth equation (Eq. 2.1);

$$C_d = D_p \ln \frac{E}{E_c} \qquad \text{(Eq. 2.1)}$$

The measured curing depth is used as a parameter for the 3D printing process. The curing depth needs to be higher than the layer thickness in order to establish good adhesion between the layers. The determination of curing depth is based on a multiple of the printing layer thickness. Currently, most curing depths in the literature range from 1.5 to 5 times the layer thickness. (27) .

2. 5 3D Printing (DLP)

As mentioned previously, Digital Light Processing (DLP) is used for 3D printing by using the photopolymerization technique. Where there are digital micro-mirrors devices (DMD) which are responsible from fully curing the resin layer at a selected time interval. The mirrors are oriented accordingly to reflect the incident light. The light that is reflected by the DMD mirrors is exposed towards the resin and the polymerization occurs. An arc lamp with a liquid crystal display panel is used as the light energy source, as it provides a broad wavelength range at an economical cost.

The process of printing one layer includes three steps. First, the UV light is exposed and the first layer is cured between the curing surface and the supporting plate. Then, the cured layer is separated from the curing surface. While this separation occurs, the supporting plate goes up and as the final step the plate moves down to the vat to start curing the next layer.

- Step 1: Solid-Solid interface is generated from the liquid-solid interface under UV illumination.
- Step 2: The separation of the solid- solid interface.
- Step 3: Generation of new liquid-solid interface (28).

The printing process occurs between the vat bottom and the cured 3D structure. From the interfacial view, the regulation of involved interfaces concerning curing influences the printing process and the printing results (28).

Figure 2.5 and Figure 2.6 shows the DLP process and the involved interfaces during the DLP process.

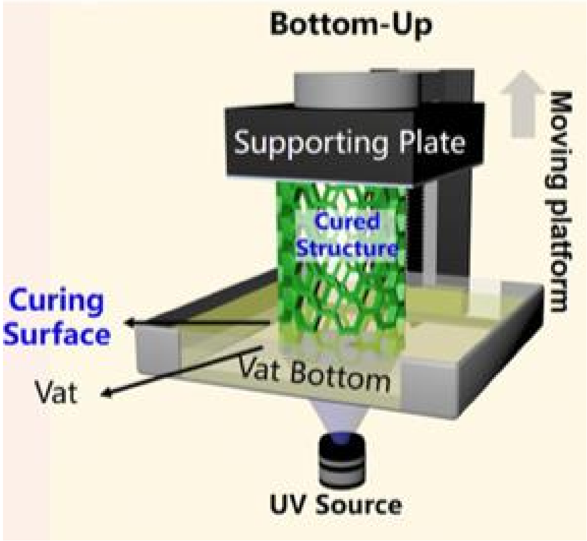

Figure 2. 5 Bottom up DLP process (28)

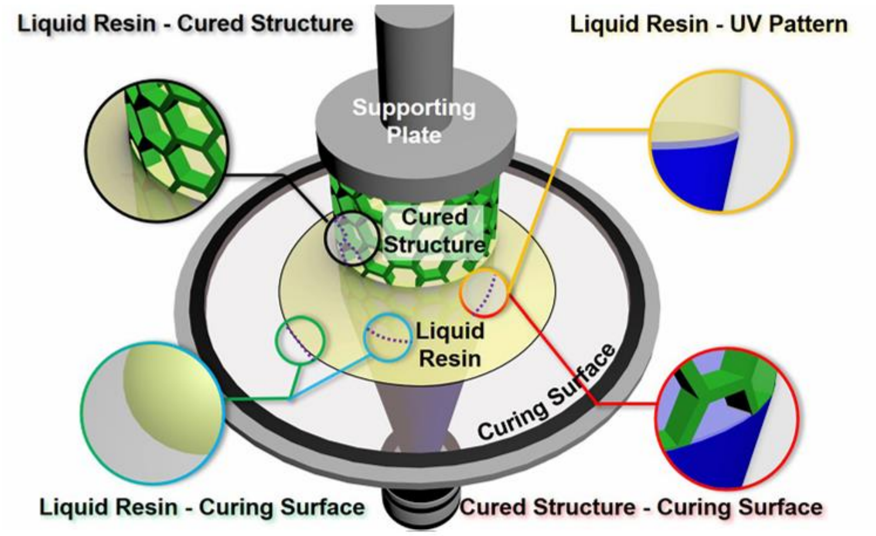

Figure 2. 6 The involved interfaces during the DLP process (28)

One of the important issues to be considered while using this for printing ceramic fabrication is the light scattering. The distribution of light in the ceramic suspension affects the monomer's conversion rate to resins. Distribution of the light is a critical parameter for the curing degree and affects the accuracy of the printed structure of the green part. In a homogenous medium without particles, the attenuation of light is typically absorption-dominated. However, the slurry contains a large amount of suspended ceramic particles and these particles will become the scattering centre of the incident light, resulting in multiple scattering (29). Because of this situation, the curing width of the slurry increases, the depth of the cure decreases and a stair stepping effect is generated. As a result, the accuracy of the 3D printing process becomes lower, the strength between the interlayer bonding becomes weaker.

In this thesis, the ASIGA 3D printer, which operates at a wavelength of 385 nm, is used for the DLP 3D printing process. The electrolyte layer is designed by using the ASIGA printer programme and the parameters regarding the thickness of each layer are selected by considering the results of the printability test. The parameters regarding this process are the curing depth, layer thickness, exposure time, exposure intensity.

2.6 Robocasting

In Robocasting (RC), the dense ceramic is obtained by the extrusion of the ceramic ink through a nozzle, driven by a pneumonic or a mechanic force. The final diameter of the deposited layer can be determined by the dimension of the nozzle.

In the robocasting technique, the control system uses a CAD model and the design of the desired layer is done by using this program. The ceramic slurry is injected in a syringe, then it is connected to the machine. In order to build a monolithic piece, the rheological properties of the ceramic slurry are crucial. In RC it is possible to control the print speed, print pressure and the filament diameter.
In this thesis, Zmorph fab multi-tool 3D printer is used for building the electrolyte layer of the PCEC and slurries made of BCZY ceramic powder are used.

2.7 Heating Stage Microscopy (HSM)

HSM is used to examine the behaviour of the printed sample when it is exposed to a temperature variation.

The HSM instrument (EM301 Heating Microscope, Hesse Instruments, Germany) is composed of the light source (halogen lamp produced by OSRAM GmbH, Augsburg, Germany), a furnace and an optical camera (The Imaging Source Europe GmbH, Bremen, Germany) which capture images of the sample during the test (Figure 2.3) (30) .

Figure 2. 7 Heating stage microscopy instrument (EM301 Heating Microscope, Hesse Instruments, Germany) (30)

Before proceeding with the analysis, the sample is placed in a Al_2O_3base and inserted inside the furnace. A camera is located in front of the furnace which is responsible for capturing the variation occurring in the shape of the sample. By using a software, it is possible to compute the reduction of the area and the shrinkage percentage. In order to start the analysis, the camera needs to be adjusted properly. A heating treatment was performed, while the heating rate was chosen as 3 °C / min and the temperature was increased from 22 °C up to 450 °C. Once the process is finished, the deformation (softening) temperature was obtained. The deformation temperature is the temperature in which the first signs of softening are detected by rounding occurring in the sample's corners.

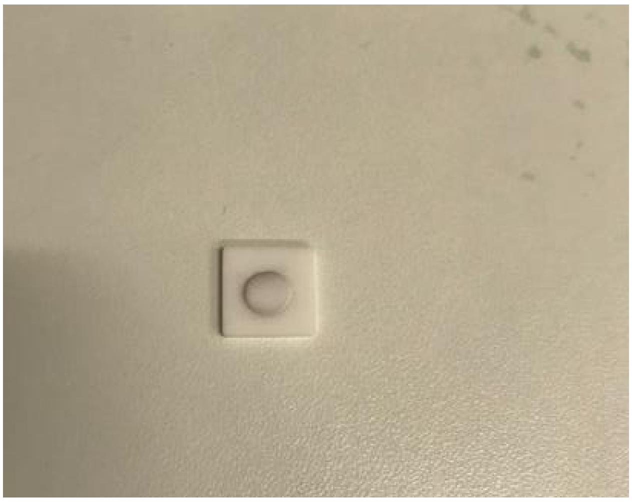

Figure 2. 8 An example of the ceramic green body used to carry out the HSM test

2.8 De-binding, Sintering

Once the ceramic green body is achieved by using the DLP and RC techniques, a thermal de-binding process is necessary to remove the organic components, such as the organic photosensitive resin component, that are present in the green body. These organic parts are burned at high temperature and the brown body part is obtained. This is followed by a sintering process in which the brown body part is transformed into a densified ceramic part. It is important to note that shrinkage occurs after the de-binding process, and surface defects, such as cracks, may develop or propagate during this stage.

In this thesis, the de-binding process was carried out with a heating rate of 1 °C/min. The thermal cycle began at 25 °C, gradually increasing to 800 °C. Once this temperature was reached, it was maintained until the temperature began to decrease back to 25 °C. The entire process lasted for 26.22 hours, using a Manfredi 1100 furnace.

For the sintering process, the heating rate was also set to 1 °C/min. The thermal cycle began at 25 °C, increasing to 1500 °C before gradually returning to 25 °C. This process lasted for 21.39 hours and was performed using a Nabertherm furnace.

2.9 SEM

Scanning electron microscopy (SEM) is a widely used technique to analyse and characterize the sample microstructure. In this thesis, the SEM analysis is used to analyse and acquire high magnification micrographs of the 3D printed electrolyte sample after the de-binding and the sintering processes were performed.

In order to perform the SEM analysis, the samples were subjected to a sputtering process to deposit platinum over the surface of the sample. After this process, the sample was placed inside the SEM device.

SEM features an electron gun that directs the electron beam onto the sample, with the beam focused using magnetic lenses in a high-vacuum environment. The interaction between the electrons and the sample produces both backscattered electrons (BSEs) and secondary electrons (SEs). BSEs are electrons that are redirected by the electric fields within the atoms, while SEs are emitted from the sample's surface. These secondary electrons are subsequently lost after colliding with the backscattered electrons. Both the BSEs and SEs are collected by the dedicated detectors. The BSEs provide information about the sample composition, topography, mass thickness and crystallography. The number of backscattered electrons is proportional to the atomic number of the atoms composing the specimen. In conclusion, with BSE imaging, it is easier to distinguish between different phases while with the SEs it is possible to provide a detailed topology of the sample (31).

Furthermore, the SEM analysis has been combined with the Energy Dispersive X-ray spectroscopy (EDX). By using the EDX, it is possible to detect the chemical elements present in a certain region and evaluate their quantity in atom%. In this thesis, this technique is used to characterize the BZY powder.

2.10 Ultraviolet-visible spectroscopy (UV VISIBLE)

UV-Visible spectroscopy is a technique used to assess the absorption of light at particular UV or visible wavelengths by a sample, in relation to a reference or blank sample. It operates within the ultraviolet and visible sections of the electromagnetic spectrum. In this thesis, UV visible analysis is conducted to analyse the photocurable slurry.

In the UV visible analysis, the sample was put in the middle of a glass which is then placed inside the machine. The light source emits the light and covers the UV and visible ranges of the spectrum. A monochromator isolates specific wavelengths of light, making sure that only one wavelength at a time is directed at the sample. As the light passes through the sample, certain wavelengths are absorbed by the molecules depending on their electronic structure. The remaining light reaches a detector, which measures the intensity of light that is transmitted through the sample and compares it to the initial intensity. This data is analysed to produce an absorption spectrum, where absorbance (A) is plotted against wavelength. Peaks in the spectrum indicate wavelengths with maximum absorption, offering insights into the sample's electronic transitions and molecular structure (32).

2.11 X-ray diffraction (XRD)

The XRD analysis was conducted to analyse the inner structure of the calcinated BZY powder.

XRD analysis relies on the constructive interference of monochromatic X-rays with the sample. X-rays are generated using a cathode ray tube, filtered to produce monochromatic radiation, and then collimated toward the sample. When the incident beam interacts with the sample, constructive and diffracted rays are produced, provided the conditions meet Bragg's Law (Equation 2.2):

$$n\,\lambda = 2\,d\,sin\theta \qquad \text{(Eq. 2.2)}$$

where θ represents the incident angle, λ is the wavelength of the beam, d is the interplanar distance, while n is the order of reflection, corresponding to the number of wavelengths in the path. Bragg’s Law connects the wavelength of electromagnetic radiation to the diffraction angle and lattice spacing in a crystalline sample.

The characteristic X-ray diffraction pattern produced during XRD analysis serves as a unique "fingerprint" of the crystals in the sample. By comparing the obtained data with the reference patterns from the ICDD database in X-Pert HighScore software, the crystalline form can be identified (31).

Chapter III

Results and Discussion

3.1 Rheological Analysis of BZCY Slurries for RC

BZCY ceramic powder was selected for this application due to its high proton conductivity and lower sintering temperature requirements. Additionally, its larger particle size compared to BZY influences viscosity, making it a key factor in the selection process.

Figure 3.1 illustrates various BZCY slurries with different solid load, dispersant, and plasticizer concentrations. All the slurries exhibit shear thinning behaviour where viscosity decreases with increasing shear rate. Additionally, as the shear rate rises, both stress and viscosity increase.

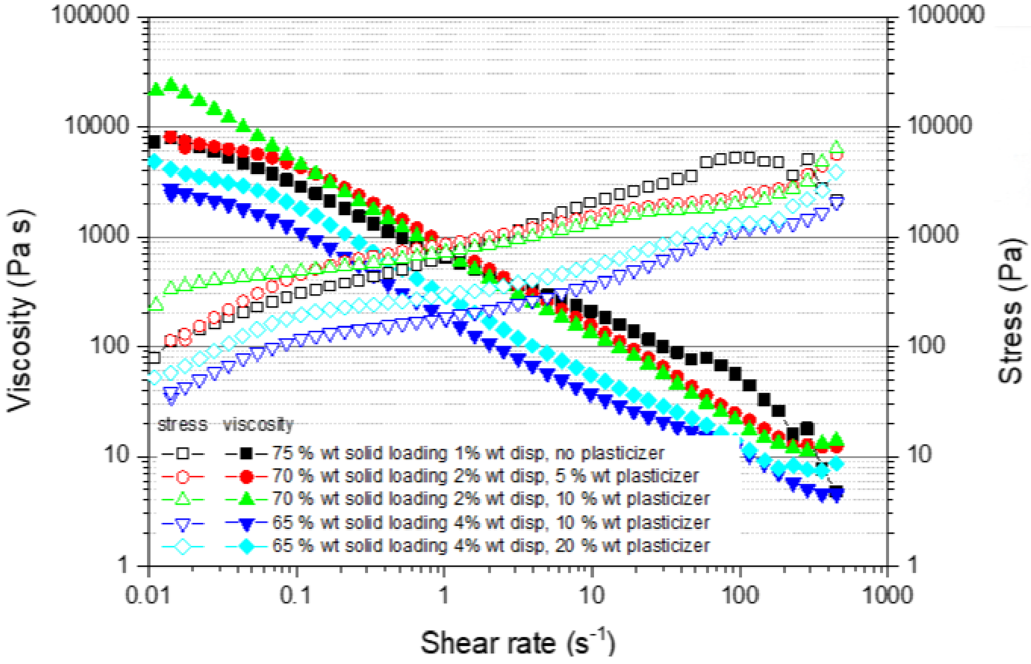

Figure 3. 1 Viscosity vs Shear rate vs Stress graph for RC slurries

It is evident that increasing the plasticizer concentration reduces the viscosity. For instance, the slurry with 70 wt% solid load, 2 wt% of dispersant and 5 wt% of plasticizer is significantly more viscous than the slurry containing 10 wt% of plasticizer. Similarly, reducing the solid load while increasing the plasticizer and the dispersant concentration further lowers viscosity.

The viscosity of the slurry is a critical factor in the RC process. During extrusion, an adequate viscosity is required to ensure smooth flow without the need for excessive force, which could damage the machine. The variations in slurry composition were primarily aimed at improving homogeneity and stability.

Each sample was processed through RC, deposited on plastic paper, and left to dry for several days. The first notable observation was that the slurry containing 75 wt% solid load, 1 wt% dispersant, and no plasticizer was the least stable. Upon drying, the sample immediately failed, developing numerous cracks.

To eliminate cracks and achieve a more stable slurry, plasticizer was added at 5 wt%, while the dispersant concentration was increased by 1 wt% and the solid load reduced to 70 wt%. However, as shown in Figure 3.2, this plasticizer concentration was insufficient to ensure complete stability.

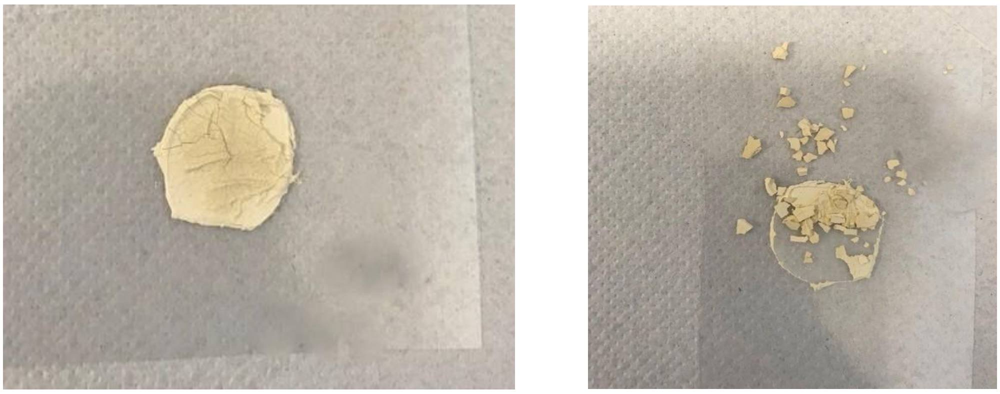

Figure 3. 2 The BZCY sample with 70%wt solid load, 2%wt dispersant, 5%wt plasticizer

Further modifications were made to obtain a more dispersed and stable slurry. First the plasticizer concentration was increased up to 10 wt% while keeping the solid load and the dispersant concentration constant. As a result (Figure 3.3) the stability improved though cracks were observed on the dried sample.

Figure 3. 3 The dried BZCY sample with 70 wt% solid load, 2 wt% dispersant, 10 wt% plasticizer

A final modification was made by increasing the plasticizer and dispersant concentrations to 20 wt% and 4 wt%, respectively, while reducing the solid load to 65 wt%. This adjustment resulted in improved stability compared to the previous attempt.

The deposition was carried out using the final modified slurry composition and the RC process on both plastic foil and an alumina plate. Figure 3.4 and 3.5 shows the sample images after the deposition.

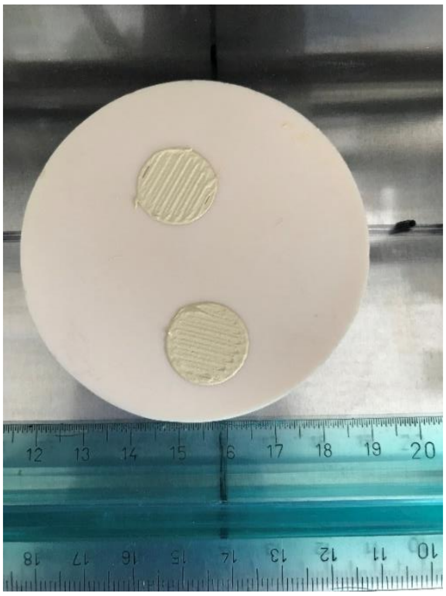

Figure 3. 4 Deposited BZCY samples on an alumina plate

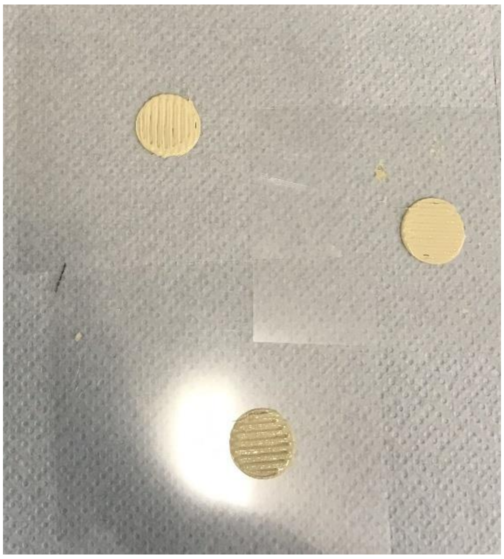

Figure 3. 5 Deposited BZCY samples on a plastic foil

After deposition, the samples were dried for a few days before undergoing the thermal process in a furnace. The samples deposited on the alumina plate were placed in the furnace for the debinding and sintering process.

One challenge with the samples deposited on plastic foil was their removal after drying, as they were difficult to detach without disturbing their shape. Although the final slurry composition improved stability, it did not fully eliminate crack formation; a possible solution could be using thermo-curable slurries for the RC process.

3.2 Analyses of the BZCY Samples After Sintering

The sintered BZCY samples are shown in Figure 3.6 a and Figure 3.6 b. As can be seen from the figure the cracks propagated during the sintering process. Also to mention that cracks were already present in the deposited green body since the final composition wasn’t fully improved the stability.

During the sintering shrinkage occurs and the particles begin to densify. The existing cracks on the BZCY samples may lead to crack growth or uneven densification.

This might also be related to the interaction between the substrate and the deposited sample. Since the deposition is made directly on the alumina plate, this might act as a constrain, this may restrict the shrinkage during sintering and leading to stress release and as a result crack propagates.

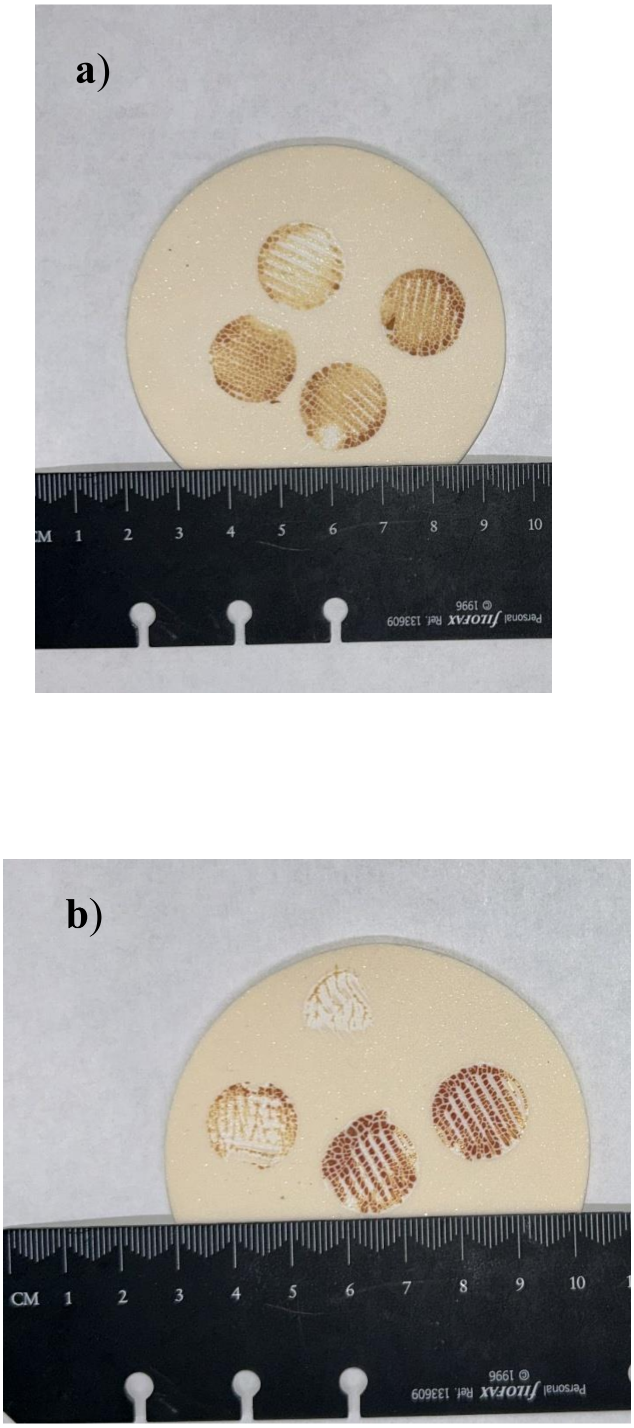

Figure 3. 6 a) and b) The Sintered BZCY samples

3.3 Slurries for vat- photopolymerization characterization

3.3.1 Characterization of BZCY vs BZY slurries

To gain deeper insight into their interactions with other slurry components, rheological behaviour, and impact on the printing process, both BZCY and BZY slurries were prepared and analysed separately. Although both powders possess a perovskite structure, they exhibit different performance characteristics.

The rheological analysis revealed that the slurry made with BZY exhibit higher viscosity compared to the slurry made with BZCY by using the same formulation.

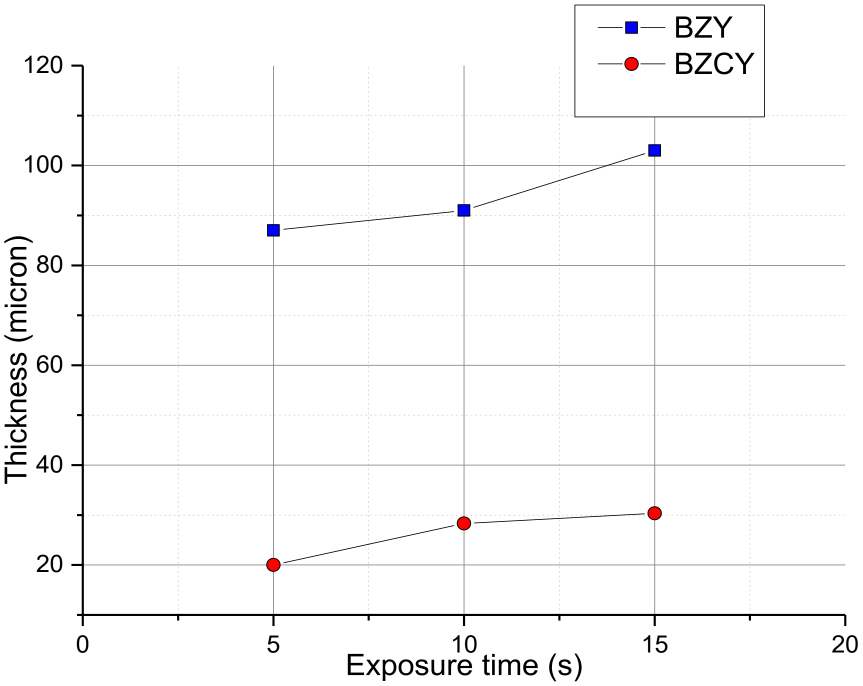

Figure 3. 7 Printability results of BZY and BZCY slurries

Further analysis was performed by doing the polymerization test. The exposure time is chosen as the 15 seconds, 10 seconds and 5 seconds and the cure depth is measured. The results are shown in Figure 3.7. As seen in the figure, the BZY slurry allows for a greater thickness. When exposed for 10 seconds, the BZY layer reaches approximately 90 microns, whereas the BZCY layer achieves only around 30 microns under the same conditions.

BZCY has proposed as a high-performance electrolyte material with many advantages such as its high proton conductivity, lower sintering temperatures compared to BZY and for its low viscosity values. However, the printability test results showed that the thickness obtained with BZCY was nearly three times lower than that of BZY. The printability test results are crucial for ensuring the accuracy of the printing process, the cure depth required to be 1.5 to 5 times greater than the layer thickness. For this reason, BZY was selected as the electrolyte material for the DLP process, and further tests were conducted using it.

3.3.2 Optimization of the resin: Impact of additives

Several factors influence the DLP process, including rheological behaviour and printability, also referred to as the polymerization. However, the most critical factor is the slurry's ability to polymerize, as polymerization is essential for forming solidified geometries. Therefore, careful preparation of the slurries is crucial to ensure successful printing.

A key factor in polymerization is the photo-initiator (BAPO), which is highly sensitive to light. If improperly handled, BAPO may deactivate, preventing polymerization and leading to print failures. Additionally, other factors such as material interactions, impurities, and slurry composition may influence polymerization efficiency.

To investigate these effects, a printability test was conducted on a BAPO and TMPTA mixture, with results presented in Table 3.1. Two additional mixtures were prepared: one incorporating PEG400 and another with Disperbyk103. All tests were performed using a 10-second UV exposure time, and results were analysed to assess polymerization efficiency.

During the experiments, polymerization failure was observed in some cases. Several potential causes were considered: 1) BAPO deactivation due to unintended light exposure, 2) chemical interactions between slurry components leading to degradation, 3) impurities in TMPTA interfering with the process, and 4) possible variations in BZY composition.

To address these concerns, TMPTA was filtered to remove impurities, and all components were tested together to evaluate their interactions. The polymerization test was repeated using a 10-second UV exposure to determine the effectiveness of these modifications.

Table 3.1 presents the printability results of the BAPO and TMPTA mixture. Additionally, two separate mixtures were prepared: one by combining PEG400 with BAPO and TMPTA, and another by mixing Disperbyk103 with BAPO and TMPTA. The same tests were conducted, 10 seconds was chosen as the exposure time, and the results are presented in the table.

Table 3. 1 The polymerization test results of the components of the slurry

	Day 1	**Day 2**
BAPO+TMPTA	437 µm	397 µm
BAPO+TMPTA+PEG400	444 µm	413 µm
BAPO+TMPTA+DISBERBYK103	387 µm	370 µm

The components were found to be compatible, and polymerization was successfully observed. While a slight decrease was noted after one day, the thickness remained sufficient for the printing process.

To further investigate the impact of filtration on printability, an additional test was conducted using two separate mixtures: one with filtered BAPO and TMPTA, and another with unfiltered BAPO and TMPTA. Both mixtures were exposed to UV light for 10 seconds. The mixture with filtered TMPTA resulted in a thickness of 452 µm, while the mixture with unfiltered TMPTA achieved a thickness of 490 µm. This suggests that the impurities present in TMPTA did not influence the polymerization process.

3.3.3 BZY Powder Characterization (SEM-EDX Analysis)

Analysis of the BZY as received powder and the calcinated BZY powder at 800°C for 6 hours were performed. Subsequently, both the calcinated powder and the as-received BZY powder from the producer were characterized using SEM combined with EDX. Figure 3.8 presents the SEM image of the as received BZY powder.

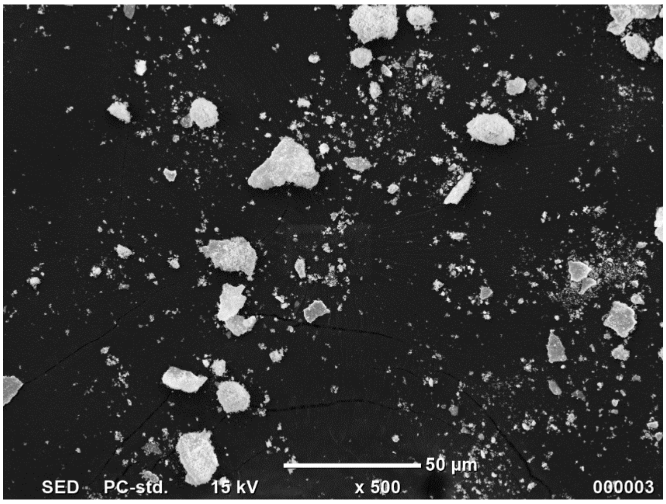

Figure 3. 8 SEM morphology of the as received BZY powder

EDX analysis confirmed the presence of Barium, Yttrium, Zirconium and Oxygen in the as received powder. The calcinated powder showed the same elemental composition, with an increase in Oxygen content, due to the removal of the volatile components. Consequently, the calcinated BZY powder was used for slurry preparation to prevent volatile components from acting as inhibitors for the polymerization and the printing process.

3.3.4 BZY Powder Characterization (XRD Analysis)

XRD analysis was conducted to investigate the crystalline structure and the phase composition of the BZY powder (as received) and BZY powder after calcination at 800 °C. Figure 3.9 and Figure 3.10 show the XRD patterns for as received and calcinated BZY powders, respectively.

In both samples, two phases were detected: cubic $BaZrO_3$ cubic as the primary phase (JCPDS card number 00-006-0399, indicated by * in the plots) and orthorhombic $BaCO_3$ as the secondary phase (JCPDS card number 00-001-0506, indicated by + in the plots).

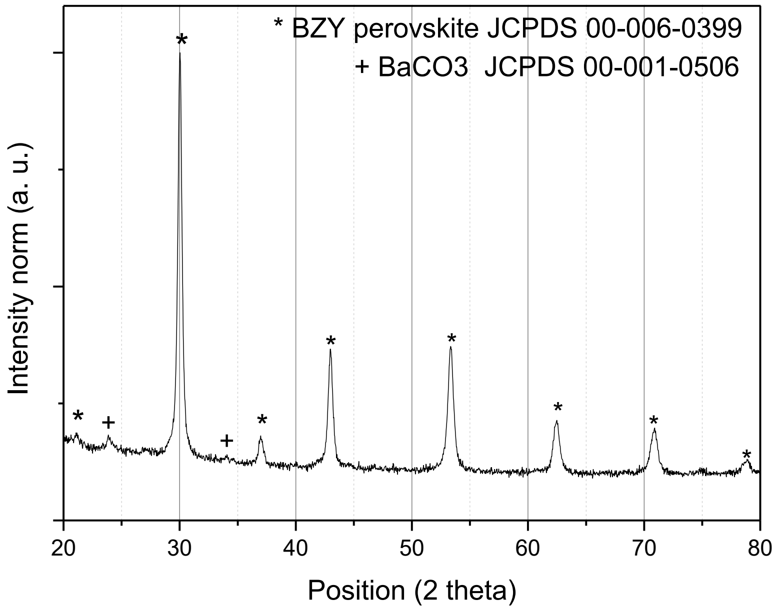

Figure 3. 9 XRD pattern of BZY powder (as received)

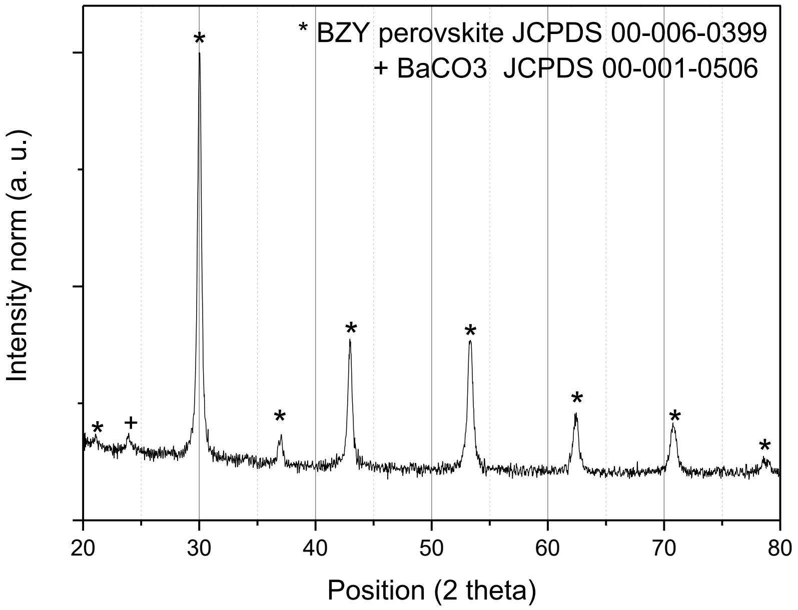

Figure 3. 10 XRD pattern of BZY powder (calcinated at 800°C)

Due to the absence of the BZY perovskite in the XPERT High-Score program database the $BaZrO_3$ structure was selected. Later, the XRD pattern of BZ was compared with that of the BZY perovskite structure, and they were found to be compatible (33).

The XRD patterns exhibit a similar trend before and after calcination, with no significant shift in peak positions. This confirms that the BZY perovskite structure remains stable after calcination.

3.3.5 UV- Visible Analysis

UV visible analysis was performed to have a deeper insight of the absorbance of the BZY powder combined with the resin; also, the dependency of the photo initiator (BAPO) concentration on the absorbance has been investigated. Figure 3.11 shows the absorbance results of the BZY, BZY calcinated at 800 °C including the different concentrations of BAPO. The operating wavelength of the ASIGA printer, 385 nm, is also represented in the figure.

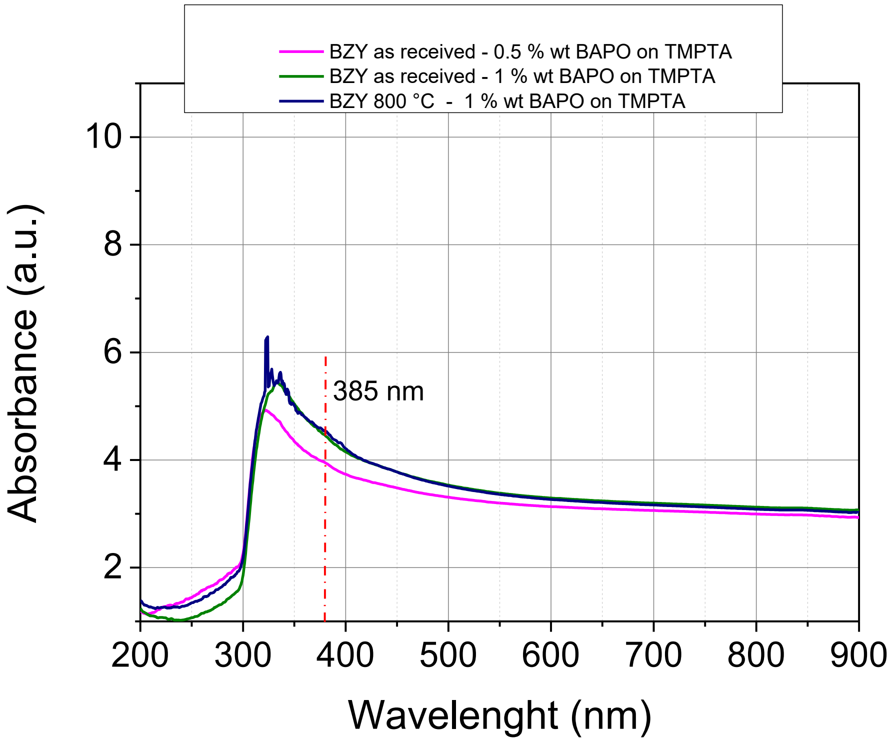

Figure 3. 11 The light absorbance vs wavelength graph of BZY powder

As can be seen from Figure 3.11, all the BZY compositions show almost no absorbance from 200 nm to 300 nm, reaching their peaks around 325 nm. After reaching the peak all the BZY compositions followed a decreasing trend until 500 nm. It is important to note that all the analysis shared a similar trend and the absorbance values are in the same range. Moreover, all compositions showed sufficient absorbance at 385 nm, which indicates the operating wavelength of the Asiga printer.

It is evident that when the photo-initiator (BAPO) concentration was doubled it improved the absorbance of the composition.

The higher absorbance values are not favourable for the DLP process. For an effective DLP, the slurries should absorb light at specific wavelengths (typically in the UV range). Excessive absorbance leads to poor light penetration during photopolymerization, resulting in curing problems such as incomplete curing (34).

The UV visible analysis revealed the significance of the photo- initiator concentration within the slurry composition. Moreover, it showed that the slurries have sufficient absorbance in the operating wavelength range of the Asiga Printer, which was used for the DLP process.

3.3.6 Optimization of Solid Loading and Plasticizer Content

The solid volume fraction and plasticizer concentration significantly influence the fluidity of UV-curable ceramic slurries. To determine the optimal composition, the viscosity of slurries with solid loadings ranging from 58 wt% to 60 wt% was assessed, while the plasticizer concentration was varied between 20 wt% and 25 wt%. The results are presented in Figure 3.12, where the black curve represents the commercial resin used as a reference.

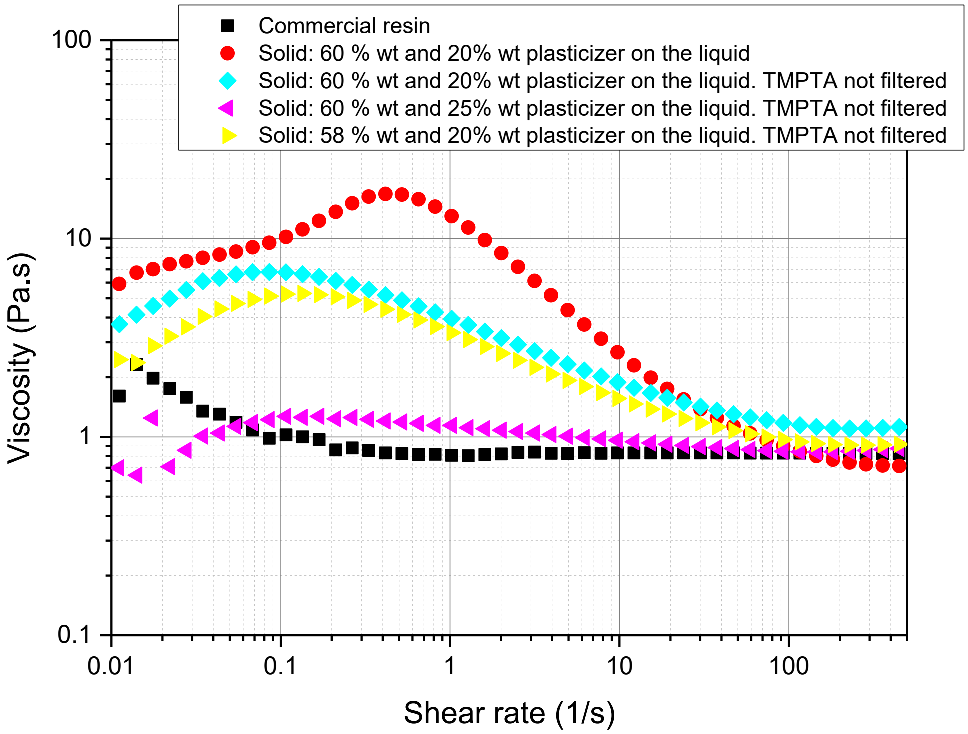

Figure 3. 12 Viscosity vs shear rate graph for the slurries

All slurries exhibited shear-thinning behaviour, with viscosity decreasing as the shear rate increased. At a shear rate of 1 s^{-1}, the flow behaviour was consistent across all samples. At 10 s^{-1}, the viscosity of the slurry containing 60 wt% BZY particles and 20 wt% TMPTA was 3.7 Pa·s, while increasing the plasticizer concentration to 25 wt% further reduced viscosity. Additionally, as the solid loading increased, viscosity also increased. The slurry with 58 wt% solids exhibited lower viscosity than the 60 wt% slurry at the same plasticizer concentration.

Considering the effects of both plasticizer concentration and solid content on fluidity, a composition of 60 wt% solid loading and 25 wt% plasticizer was selected. This formulation closely follows the viscosity trend of the commercial resin, making it suitable for DLP technology, where achieving high solid loading with low viscosity is essential.

3.3.7 Evaluation of Polymerization and Cure Depth

Each sample underwent a polymerization test, and the thickness of the polymerized pieces was measured. This step is crucial for determining the appropriate layer thickness in the DLP printing process. In general, the curing depth of ceramic slurries is influenced by the average particle size of the ceramic powder, the concentration of ceramic particles, light scattering effects, and the energy density of the light source.

The evaluation of the effect of different solid fraction and plasticizer concentration on curing depth can be seen in Figure 3.13. The slurries were cured at varying exposure times 5,10 and 15 seconds. The curing depth of all suspensions increased as the exposure time (energy dose) increased. However, no clear relationship is observed between the plasticizer concentration and the curing depth of the ceramic slurry.

It can be said that at low plasticizer concentrations, the slurry exhibits poor dispersion stability of the ceramic particles, leading to variations in the measured curing depth.

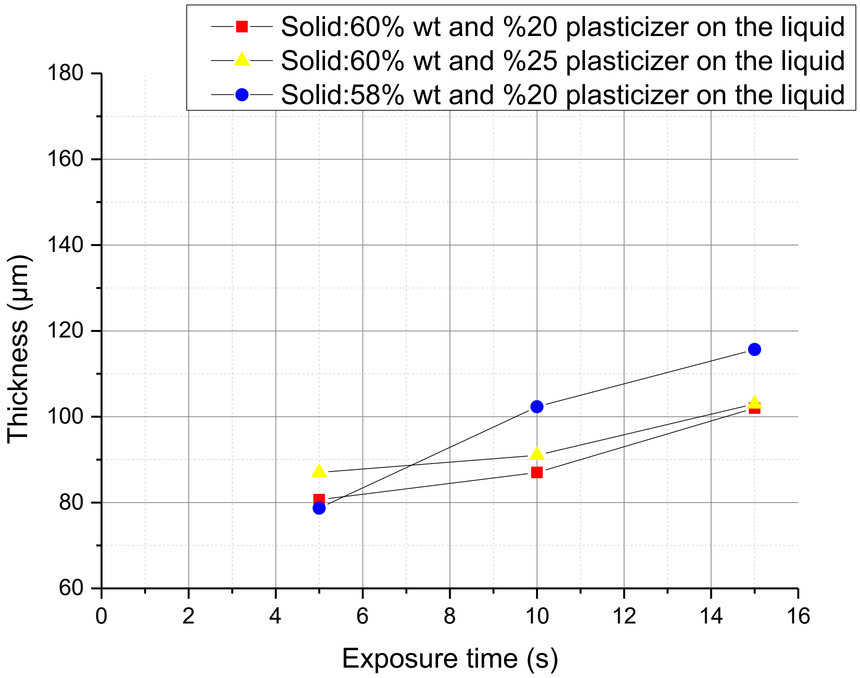

Figure 3. 13 Thickness vs Exposure time graph of slurries with different composition

Two important observations were made during the polymerization test. The first was the occurrence of shadowing on the printed samples as the exposure time increased. This effect became more pronounced at longer exposure times. Shadowing is directly related to light scattering phenomena within the slurry.

The slurry contains a large number of suspended BZY ceramic particles, and the particle size significantly influences light absorption and scattering. When UV light propagates through the slurry, multiple scattering events occur due to the presence of ceramic particles. The scattered light is not lost, it changes direction and penetrates into areas where the curing is not wanted. This leads to excessive curing at the edges of the exposed area, negatively impacting both the accuracy and mechanical strength of the printed structure (35).

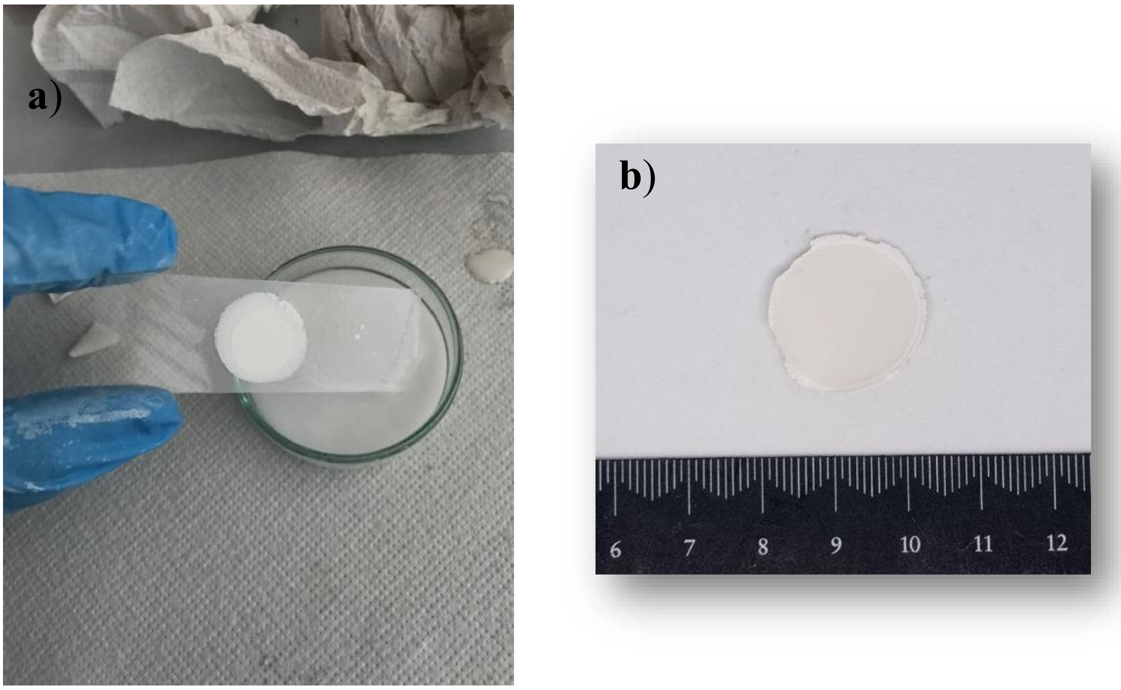

Figure 3. 14 Shadowing around the polymerized sample; a)20- and b)15-second exposure times

As exposure time increases, the slurry is subjected to more light, resulting in greater scattering. This, in turn, causes increased polymerization at the edges of the desired object, further amplifying the shadowing effect. Figure 3.14 illustrates the shadowing observed during the polymerization test at a) 20- and b)15-second exposure times, respectively.

The second observation concerns the non-homogeneity of the slurry, which is a critical factor in the DLP process, as it directly impacts the precision of the printed layers. This issue is closely linked to the first observation, emphasizing that achieving a uniform slurry distribution is essential for successful DLP printing.

As shown in Figure 3.15, agglomerations are present on the polymerized pieces, leading to light scattering and multiple refractions, which introduce errors in the final print. To mitigate this issue and achieve more effective polymerization, the dispersant in the slurry can be modified, or its concentration can be increased to improve particle distribution.

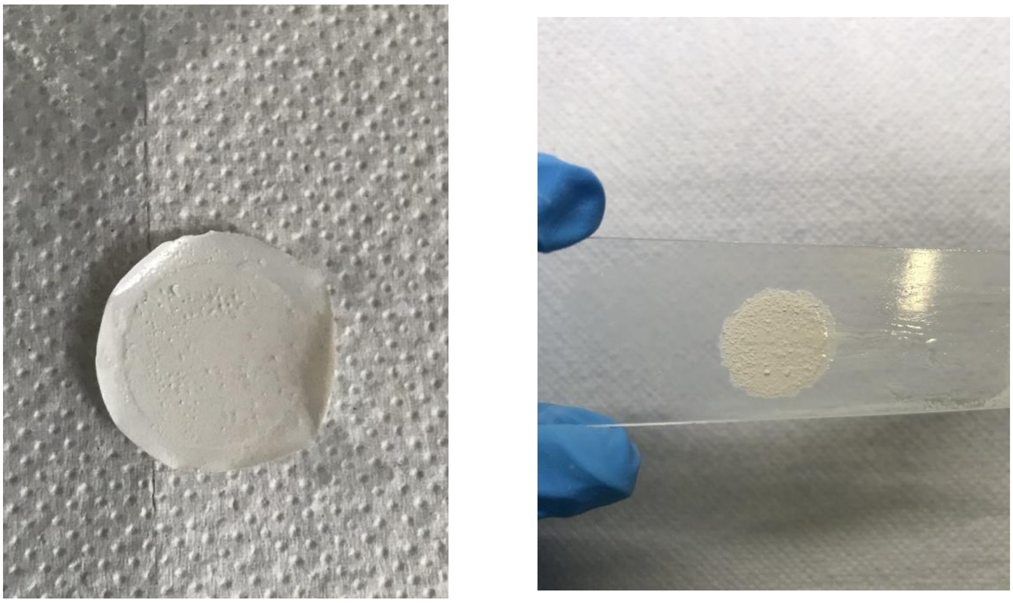

Figure 3. 15 Agglomerations on the polymerized pieces

Figure 3.16 illustrates the effect of the calcination temperature on the cure depth. As shown in figure, higher calcination temperatures result in greater cure depth thickness. This can be attributed to the impact of calcination temperature on the particle size of the BZY powder.

Calcination is a thermal process in which particles tend to fuse together at elevated temperatures, leading to grain growth and an overall increase in particle size. As a result, slurry containing 25 wt% plasticizer and BZY calcined at 1200°C achieves a cure depth of up to 130 µm after 10 seconds of UV exposure. In contrast, slurry with the same composition but BZY calcined at 1000°C reaches only 100 µm under the same exposure conditions.

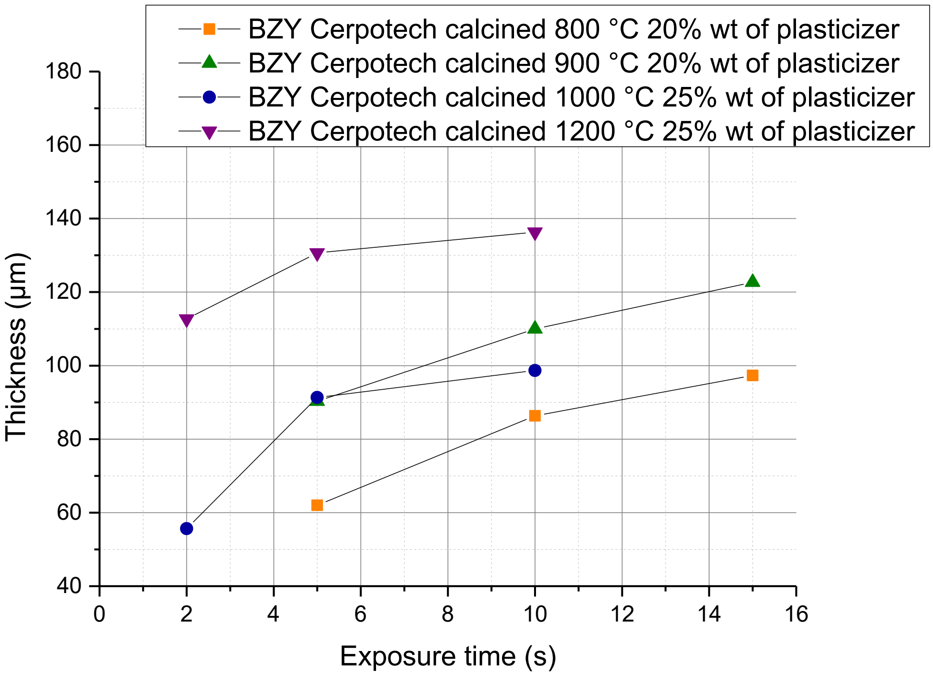

Figure 3. 16 Thickness vs Exposure time graph of slurries with different calcination temperature

The increase in BZY powder particle size positively affects light scattering, as larger ceramic particles have a lower surface area and fewer interfaces, reducing scattering and allowing more light to pass through the slurry. However, the particle dispersion within the slurry was not uniform, resulting in agglomerations in both the slurry and the polymerized pieces (Figure 3.17).

Agglomeration may have occurred due to the calcination process, as high-temperature treatment can cause particles to fuse together, forming large clusters.

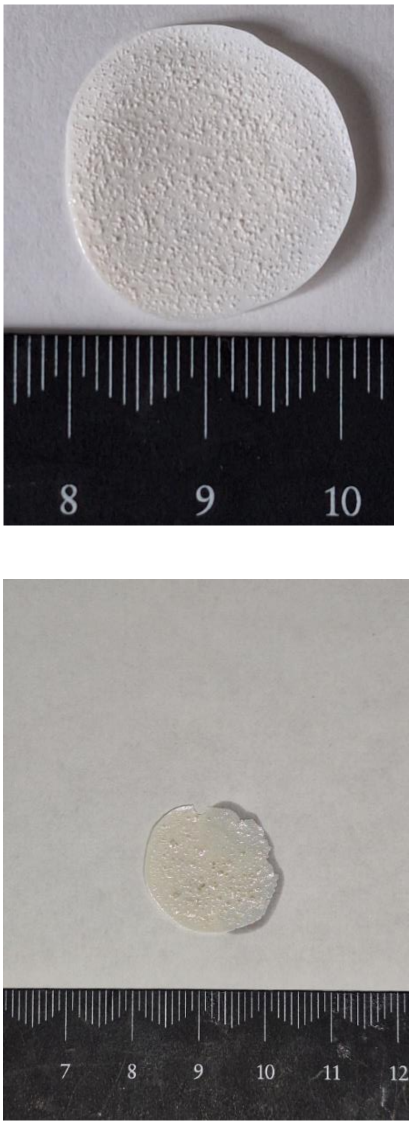

Figure 3. 17 Agglomerations on the polymerized pieces (BZY calcinated at 1000°C)

3.3.8 Effect of different monomers on slurry fluidity and cure depth

A further study was conducted to analyse the effect of different monomers on slurry fluidity. Two monomers, PEGDA 250 and HDDA, were tested while keeping all other components constant. The optimized formulation, previously determined, was used for these slurries, maintaining a solid fraction of 60 wt% and a plasticizer concentration of 25 wt%. Rheological analysis was performed, and the results are presented in Figure 3.18.

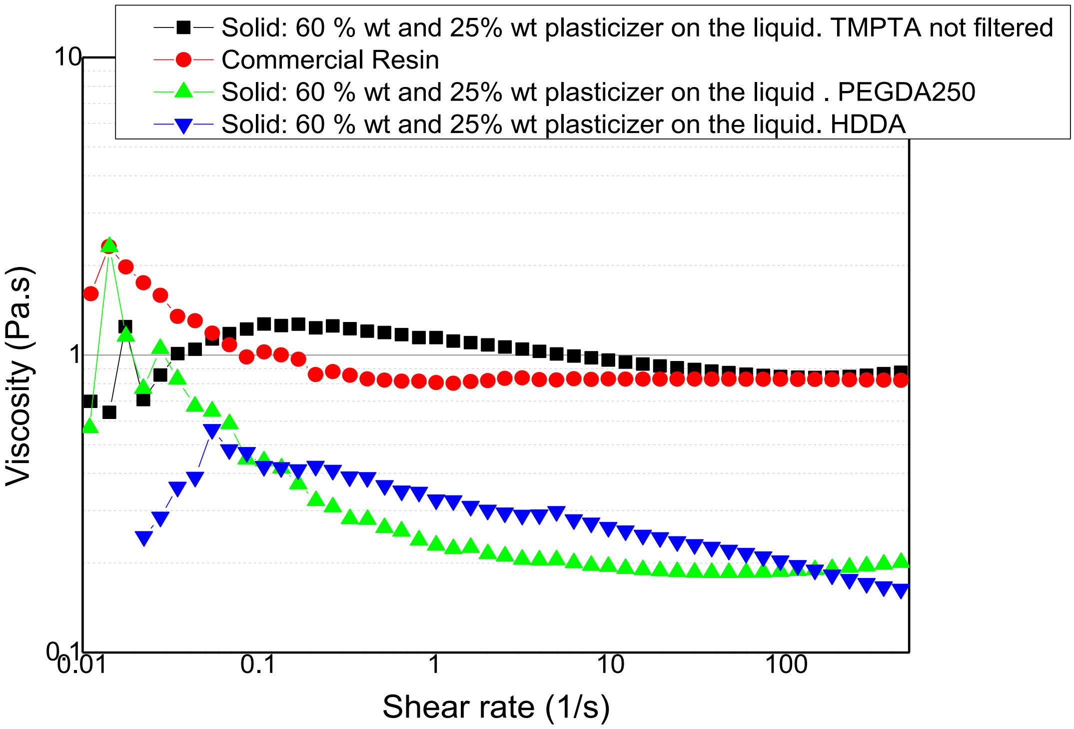

Figure 3. 18 Viscosity vs shear rate graph for the slurries made with TMPTA, PEGDA250 and HDDA

As shown in Figure 3.18 it is evident that the highest viscosity was found for the slurry containing TMPTA, follow by PEGDA250 slurry and the lowest for HDDA slurry. This is probably due to higher molecular weight of TMPTA ($M_n = 296$) compared to PEGDA250 ($M_n = 256$) and HDDA ($M_n = 226$).

During the DLP process, ceramic slurries must achieve adequate cure depth to ensure strong adhesion between the two cured layers. The impact of monomers with varying functionalities on cure depth was examined. Slurries containing HDDA, PEGDA250, and TMPTA were exposed to UV light for 3, 5, 10, and 15 seconds, after which their thickness was measured. The results of the polymerization test are presented in Figure 3.19.

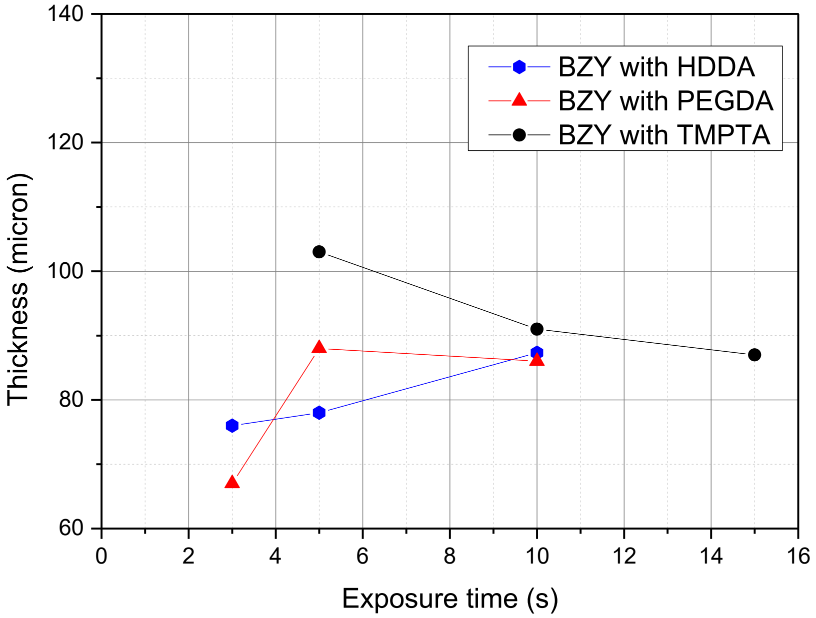

Figure 3. 19 Thickness vs exposure time of slurries made by using different monomers

The measured thickness of slurries formulated with PEGDA250 and HDDA was lower compared to those made with TMPTA. At an exposure time of 10 seconds, both HDDA and PEGDA250 slurries exhibited a thickness of 88 µm, which is sufficient for the printing process.

Two key factors influence the cure depth of the ceramic suspension. The first is the refractive index (RI) contrast between the ceramic powder and the monomer. A higher contrast leads to increased light scattering, which reduces the cure depth and negatively impacts lateral resolution (35). Since the refractive index of the ceramic powders and the compatibility between the monomer plays a significant role in curing behaviour, optimizing this parameter is crucial for achieving precise layer formation.

The second factor is the theoretical functionality of the monomer, which refers to the number of reactive sites available for polymerization (34). TMPTA has a theoretical functionality of 3, whereas HDDA and PEGDA250 have a functionality of 2. The polymerization experiments demonstrated that an increase in functionality of the monomer can significantly increase the cure depth of the suspension.

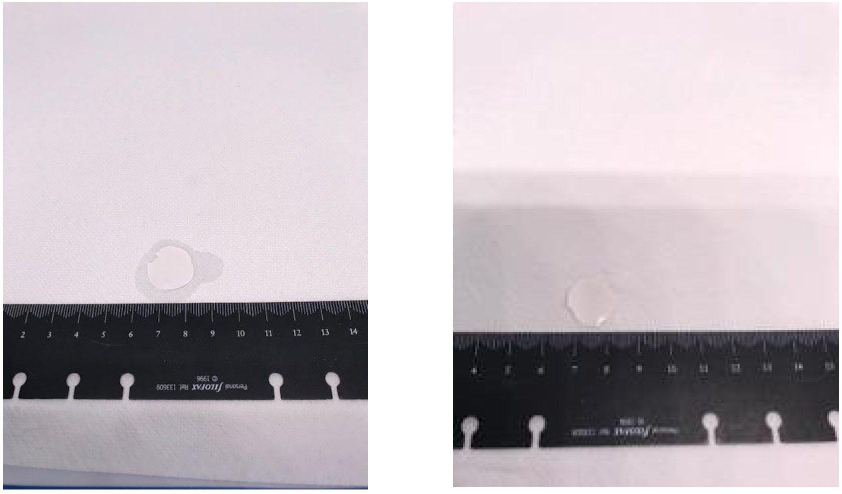

Figure 3. 20   Slurry with TMPTA after the polymerization test (10 and 5 seconds)

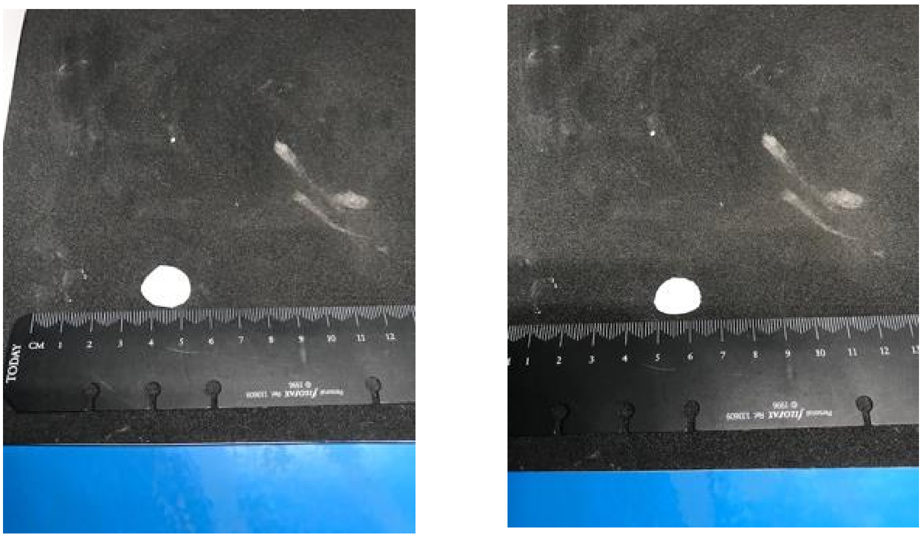

Figure 3. 21 Slurry with HDDA after the polymerization test (10 and 5 seconds)

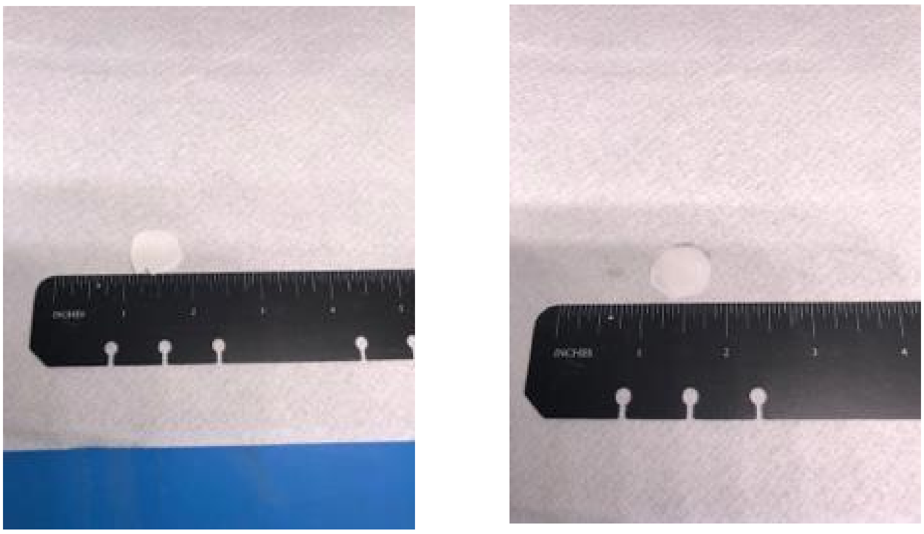

Figure 3. 22 Slurry with PEGDA250 after the polymerization test (10 and 5 seconds)

3.4 Analysis of the DLP Printing Process and Results

The optimization of printing parameters is crucial for achieving high-quality 3D DLP-printed parts. Key parameters include layer thickness, curing depth, laser power, scanning speed, and exposure intensity, among others. These factors directly influence both the dimensional accuracy of the printed structures and the overall manufacturing efficiency.

The choice of layer thickness is determined based on the results of the polymerization test, ensuring that it is 1.5 to 5 times lower than the cure depth. For the printing process, a layer thickness of 40 µm was selected. A slurry composed of TMPTA as the monomer, 60 wt% solid loading, and 25 wt% plasticizer was prepared and used for printing.

The layer thickness was set to 40 µm, with a total of 14 layers. A 600 µm disk was designed and programmed for printing. While it was possible to obtain layers, an error occurred, causing the process to be interrupted halfway. The thickness of the printed sample was measured as 240 µm. (Printed samples are shown in Figure 3.23)

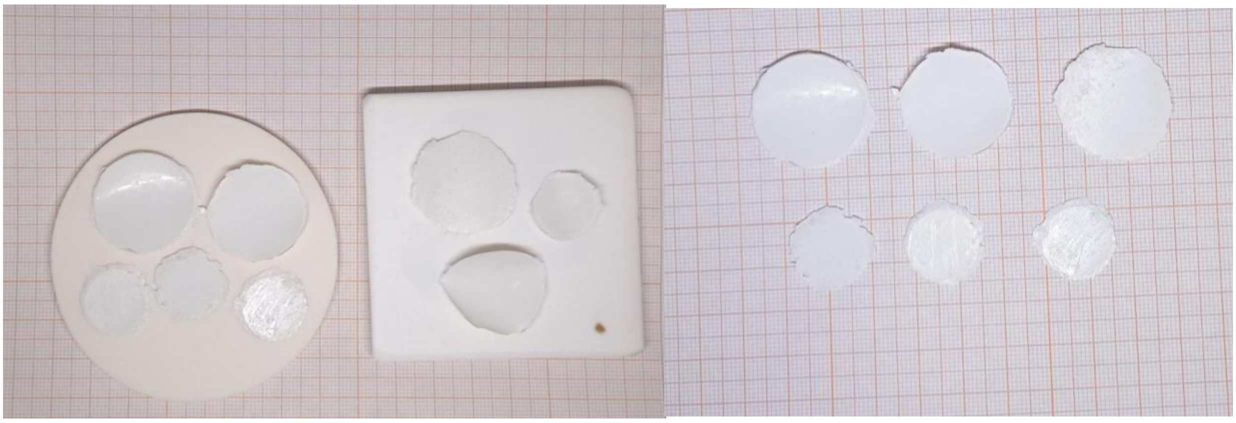

Figure 3. 23 Printed Samples by using TMPTA and BZY

This issue may be attributed to the small particle size of the BZY powder (30–100 nm, taken from the Cerpotech datasheet). The cured layer forms due to light attenuation, which leads to absorption. However, as particle size decreases, absorbance also decreases, making UV absorption less effective.

In the case of the BZY slurry, the suspended ceramic particles significantly disrupt the photopolymerization process due to light scattering. The presence of non-uniformities in the medium alters the direction of light, further impacting polymerization. Smaller particle sizes also cause greater broadening in the penetration profile, reducing the effective energy available for vertical penetration.

Another factor that may contribute to the error is the difference in refractive index (RI) between the BZY particles and the monomer. The RI is not constant and varies across different wavelengths. Most monomers have an RI of approximately 1.5, while BZY particles have an RI of around 2.2 (29). This contrast in refractive indices leads to increased light scattering, further disrupting the polymerization process.

Moreover, another printing attempt was conducted using a slurry composed of HDDA as the monomer, 60 wt% solid loading, and 25 wt% plasticizer. During the process, an interesting observation was made: while the slurry successfully polymerized and achieved a cure depth of approximately 85 μm under 10 seconds of UV exposure, it failed to print the desired object.

To resolve this issue, the printing parameters on the Asiga printer were adjusted, specifically by increasing the layer thickness. As a result, a three-layered object was successfully printed, as shown in Figure 3.24, with a final measured thickness of approximately 200 μm.

However, sedimentation and agglomeration of particles were observed in the slurry, negatively impacting the printing process by disrupting the distribution of UV light during curing.

This issue arose due to the interaction between the HDDA monomer and BZY ceramic particles. While HDDA possesses excellent overall properties, it is hydrophobic, whereas BZY ceramic powder exhibits hydrophilic behaviour. As a result, their incompatibility led to particle instability, causing sedimentation and agglomeration within the slurry (36).

Additionally, another issue observed was the poor adhesion between printed layers, indicating weak interlayer bonding strength. To address these challenges, the dispersant in the slurry composition can be modified to enhance slurry stability and improve the compatibility between the BZY powder and the HDDA monomer.

Figure 3. 24 Printed Samples by using HDDA and BZY

3.5 HSM Analysis of the BZY Parts

The printed BZY sample was conducted to HSM analysis. Figure 3.25 shows the temperature increase vs the shape factor which indicates how the sample cross-section area of the sample changes as the temperature increase.

As can be seen from Figure 3.25, when the temperature is low, the thermal energy provided to the sample does not allow a change on the ceramic sample in terms of size and shape. Once the softening point is reached at 56 °C, the sample begins to soften, leading to observable shape changes. After that the shape factor started to decrease until 80°C after which it remains relatively constant until 170 °C, where a sharp reduction occurs. The shape factor then stabilizes until 300 °C. However, at 320 °C, it reaches its lowest value.

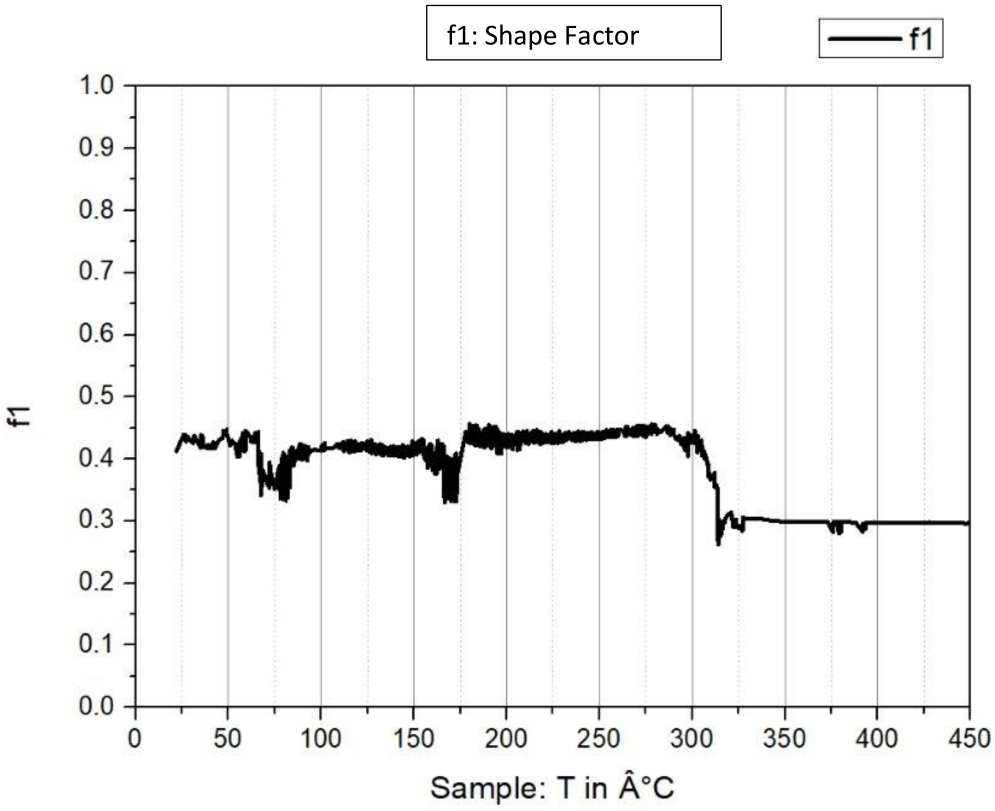

Figure 3. 25 Shape Factor vs Temperature

HSM analysis determined the softening temperature of the BZY ceramic sample to be 56 °C. Figure 3.26 illustrates the shape evolution of the sample as a function of temperature. Notably, warping begins at 320 °C, with further deformation becoming more pronounced at 450 °C. Beyond this point, the ceramic sample undergoes significant structural changes, indicating that temperatures exceeding 450 °C may lead to severe deformation.

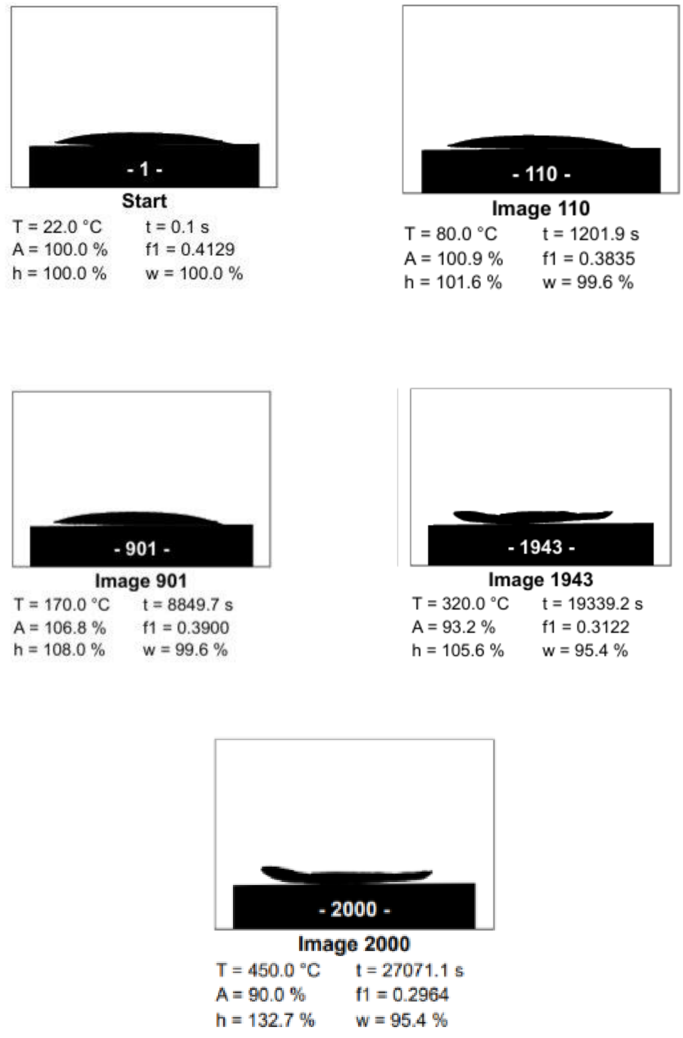

Figure 3. 26 Effect of Temperature on the Shape of the Sample

3.6 Impact of Debinding and Sintering Process on the Green Body

Figure 3.27 and Figure 3.28 shows the green bodies produced by the DLP process after undergoing debinding and sintering. The debinding process was conducted at 800°C, while sintering was carried out at 1500°C, both with a heating rate of 1°C/min.

The sintered body exhibited significant volumetric shrinkage, leading to warping. The shrinkage first occurs during debinding due to the decomposition of the photosensitive polymer resin. The ceramic part obtained after debinding exhibits poor mechanical properties, such as low density and high internal porosity.

Sintering aims at improving the microstructure and physical properties (such as bulk density and porosity) of the brown body (the object obtained after debinding) and sintering temperature has a great influence on the final mechanical properties of the ceramic parts.

In sintering, volumetric shrinkage is influenced by powder particle size and final sintering temperature, which together determine diffusion phenomena occurring during thermal treatment (37).

One interesting observation made was; some samples exhibit warping while some didn't. This might be related to uneven curing. Since during the printing process errors occurred, mainly due to the light scattering phenomena, uneven curing might have occurred in the green bodies leading to inadequate bonding between layers, negatively impacting the adhesion between layers. The stress that is released due to the volumetric shrinkage may accumulate causing the warping of the ceramic parts.

Therefore, SEM analysis must be conducted to further examine the final microstructure of the ceramic parts in greater detail. This will provide deeper insights into the effects of the sintering conditions on the material's structure and help identify potential steps for improving the mechanical properties.

Figure 3. 27 Sintered BZY samples showing Warping

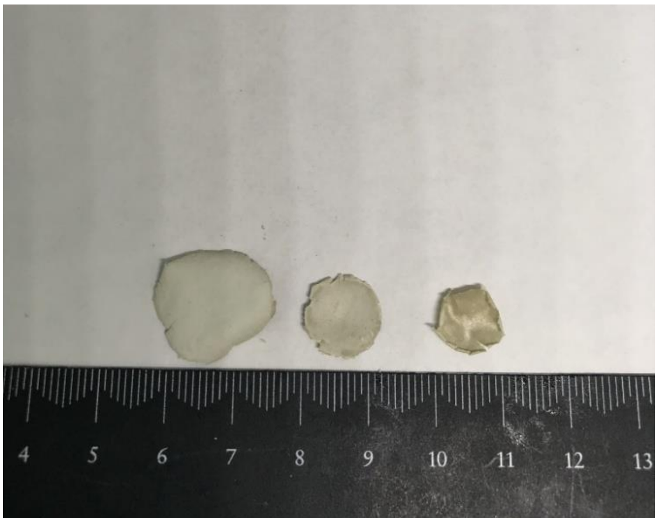

Figure 3. 28 The sintered BZY samples

3.7 Characterization and microstructure of DLP 3D-printed BZY ceramic

The surface microstructure characteristics of the sintered BZY samples were analysed by SEM. The microstructure of the ceramic part consists of grains, grain boundaries, pores and defects. The samples were platinum coated to improve conductivity before the SEM analysis were conducted.

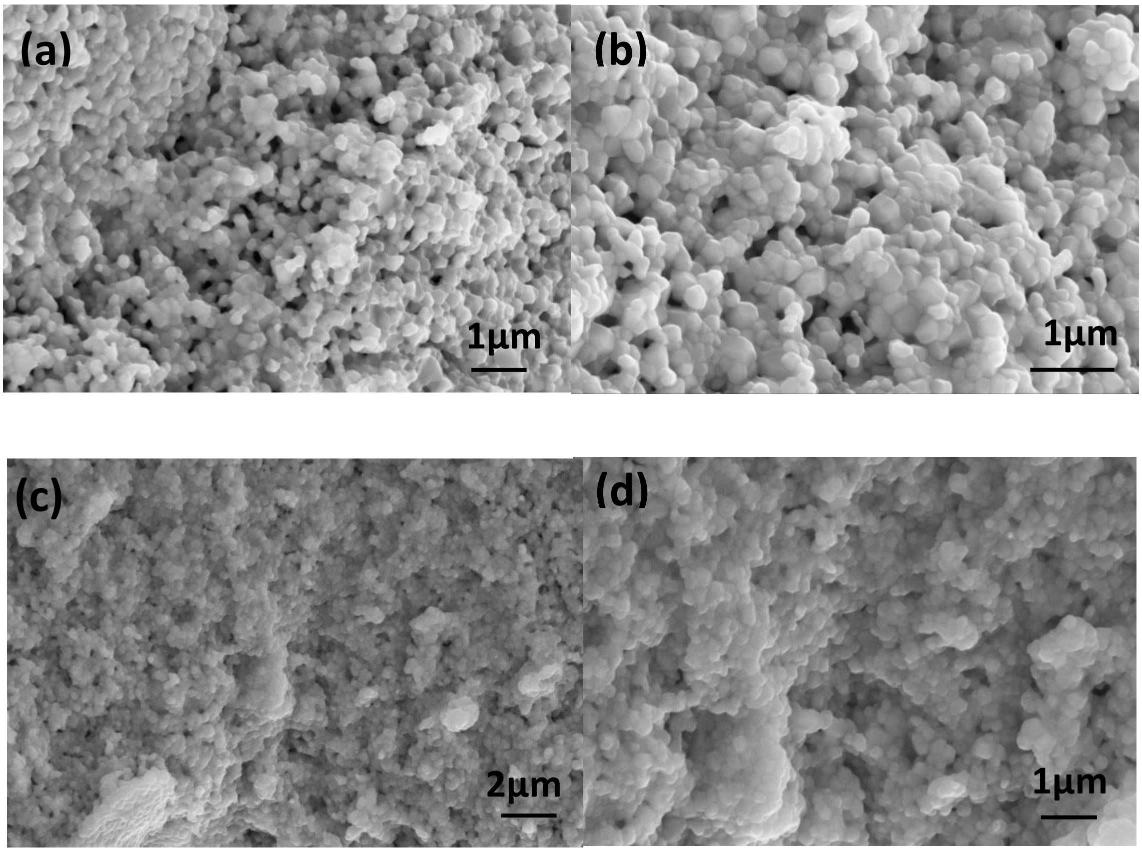

Figure 3. 29 The microstructure of the sintered BZY samples (top view), (a) 1 µm with 20 kx magnification (b)1 µm with 30 kx magnification (c) 2 µm with 5 kx magnification (d) 1 µm with 10 kx magnification

SEM image in Figure 3.29 (a) and was taken at 20000 x magnification by using 15 kV accelerating voltage while in (b) the magnification was increased to 30000 x.

It is observed that the grain size distribution wasn't uniform and during sintering grain growth showed variations also to mention that the ceramic part wasn't fully densified and examined porous structure, can be clearly seen in Figure 3.29 a and b.

Two factors might affect this situation: The first factor is related to the BZY powder. The size of the particles and its distribution among the slurry, homogeneity, agglomerations are the main causes.

The second factor is related to insufficient sintering temperature, time and heating, cooling rate. Sintering temperature significantly influences the physical properties of ceramics, increasing it can enhance densification and reduce porosity. This occurs due to the reduction in the liquid-phase viscosity, which facilitates the filling of empty pores, leading to higher density. Consequently, increased densification improves the mechanical properties, such as strength and hardness.

Therefore, excessively high sintering temperatures may lead to grain coarsening, which can negatively impact material properties and should be carefully controlled. In order to avoid this, sintering aids can be used. Sintering aids can improve the densification, reduce the porosity while reducing the sintering temperature.

Potential sintering aids that can be used to enhance the densification of BZY ceramics are: CuO, NiO, and ZnO. These additives promote grain growth and reduce porosity, leading to improve densification of the BZY ceramic parts. However, their potential impact on electrolyte conductivity should be considered in future studies (38).

The cross-section view of the BZY ceramic parts were also investigated by SEM analysis. Figure 3.30 illustrates the microstructures, (a) and (c) was taken at 1 kx magnification by using 20 kV accelerating voltage while in (b) the magnification was 800 x and in (d) it was 5 kx.

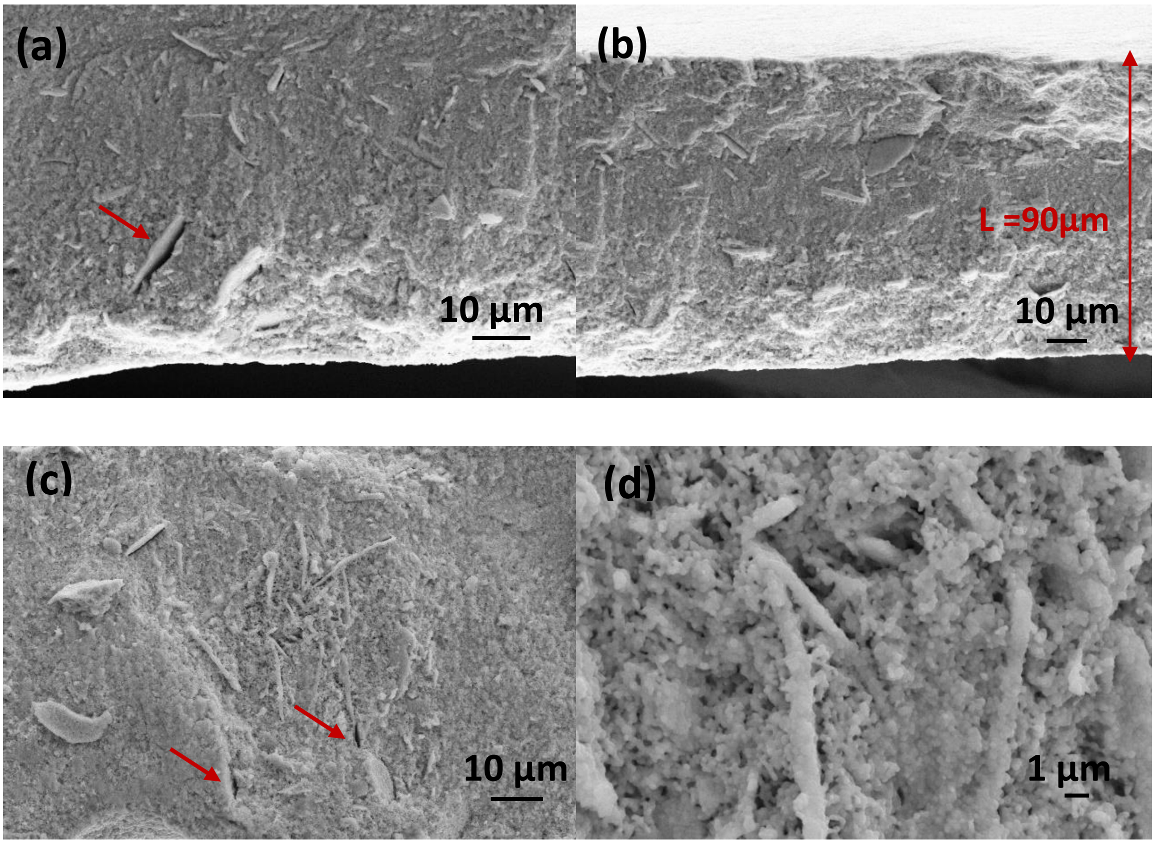

Figure 3. 30 The microstructure of the sintered BZY samples (cross section), (a) 10 µm with 1 kx magnification (b)10 µm with 800 x magnification (c) 10 µm with 1 kx magnification (d) 1 µm with 5 kx magnification

The cross -section microstructure exhibit cracks and grains. In Figure 3.30 (d) the non-uniform grain size distribution can be seen, the pores are also present. The thickness (L) of the sintered printed BZY sample was measured as 90 µm (Figure 3.30 (b)).

The 3D printed BZY samples exhibits laminar features due to layer-by-layer stacking process. The stacking process influences the interlayer cracks, which are considered as critical defects in ceramic DLP printing.

As seen in Figure 3.30 (a) and (c), interlayer defects are present in the samples, with visible cracks. These defects likely originate during the debinding process, where shrinkage induces stress concentrations at layer interfaces, leading to crack formation. Furthermore, the stress generated during sintering may further propagate these cracks.

The presence of interlayer cracks also contributes to pore formation, affecting the final properties of the sintered BZY samples. As shown in Figure 3.30 (d), a porous structure is evident.

A potential cause of these defects could be uneven UV curing during the DLP process, which weakens interlayer bonding and makes the samples more susceptible to cracks and porosity.

To mitigate these issues, adjustments to the printing parameters (e.g., exposure time, layer thickness) and slurry formulation modifications (to enhance light absorption and polymerization efficiency) should be considered. Optimizing these factors could improve interlayer bonding and reduce defect formation in the final ceramic parts.

CHAPTER IV

Conclusions

In this study, the potential of additive manufacturing (AM) techniques, specifically vat-photopolymerization DLP and Robocasting (RC), was explored to print electrolyte layers for Protonic Ceramic Electrolysis cells (PCECs) operating at 600 °C.

For the RC process the BZCY slurry composition was optimized to improve the stability and homogeneity. Although the composition with 20 wt% plasticizer, 4 wt% dispersant, and 65 wt% solid load improved stability, it was not sufficient to eliminate crack formation in the dried samples. Additionally, sintered BZCY samples showed crack propagation due to pre-existing cracks. To enhance stability, future work should focus on investigating photocurable slurries, which could offer improved performance.

For the DLP process, optimizing the BZY slurry was crucial. The composition, with 60 wt% solid fraction and 25 wt% plasticizer, exhibited lower viscosity and sufficient cure depth for the printing process. However, challenges related to particle dispersion and agglomeration caused light scattering and uneven curing, leading to reduced shape accuracy. To address this issue, future investigations should focus on identifying a compatible monomer formulation for the BZY ceramic particles to achieve a more stable, dispersed slurry composition.

The sintered BZY samples were analysed using SEM, revealing porous microstructures, low density, and non-uniform grain growth, with cracks present in the cross-sections. To improve the physical and mechanical properties of the final ceramic parts, future research could explore increasing sintering temperature or adding sintering aids such as CuO, NiO, or ZnO. Additionally, improving slurry composition could positively impact microstructure, particularly in reducing defects related to the DLP process and cured layer interfaces.

Overall, while both AM techniques show promise for producing high-performance ceramic parts with complex geometries and high dimensional accuracy, challenges remain in achieving a stable, homogeneous slurry composition. Future work should focus on improving monomer formulations and optimizing ceramic powder properties to address these issues. Moreover, further research is needed to explore the interaction between light and the ceramic slurry to better understand how layer thickness, curing depth, and curing characteristics influence the final part quality. With continued advancements, AM has the potential to significantly enhance the fabrication of advanced ceramic components for energy applications such as PCECs.

Bibliography

1. **IEA.** *«Global Energy and Climate Model Documentation».* s.l. : IEA, 2024.

2. **IRENA.** *Green hydrogen strategy design .* s.l. : IRENA, 2024.

3. **IRENA.** *Green Hydrogen:A guide to policy making.* Abu Dhabi : IRENA, 2020.

4. *Review of Hydrogen Storage Technologies and the Crucial Role of Environmentally Friendly Carriers.* **Fang, Weijie.** s.l. : American Chemical Society, July 11, 2024.

5. **IEA.** *Global Hydrogen Review.* s.l. : IEA, 2023.

6. *An overview of water electrolysis technologies for green hydrogen production.* **S. Shiva Kumar, Hankwon Lim.** s.l. : Energy Reports, 2022, Vol. Volume 8. https://doi.org/10.1016/j.egyr.2022.10.127..

7. *Nickel oxide water electrolysis diaphragm fabricated by a novel method.* **Takashi Ohmori, Kenjiro Tachikawa, Katsuyuki Tsuji, Katsuhiro Anzai.** Issue 18, s.l. : International Journal of Hydrogen Energy, 2007, Vol. Volume 32. https://doi.org/10.1016/j.ijhydene.2007.07.055.

8. *Current trends in the description of lanthanum strontium manganite oxygen electrode reaction mechanism in a high-temperature solid oxide cell.* **Michal Carda, Daniel Budáč, Martin Paidar, Karel Bouzek.** s.l. : Current Opinion in Electrochemistry, 2022, Vol. Volume 31. https://doi.org/10.1016/j.coelec.2021.100852.

9. *Alternative and innovative solid oxide electrolysis cell materials.* **Aziz Nechache, Stéphane Hody.** s.l. : Renewable and Sustainable Energy Reviews, 2021, Vol. Volume 149. https://doi.org/10.1016/j.rser.2021.111322..

10. **IRENA.** *Green Hydrogen Cost Reduction.* Abu Dhabi : IRENA, 2020. ISBN: 978-92-9260-295-6.

11. *High Temperature Electrolysis .* **Laura Almar, Sonia Escolástico, Laura Navarrete, David Catalán-Martínez.** Zaragoza : Springer, 2023, Vol. Volume 95. https://doi.org/10.1007/978-3-031-22508-6.

12. *Proton conducting oxides: A review of materials and applications for renewable energy conversion and storage.* **J. Kim, S. Sengodan, S. Kim, O. Kwon, Y. Bu, G. Kim.** s.l. : Renewable and Sustainable Energy Reviews, 2019, Vol. Volume 109. https://doi.org/10.1016/j.rser.2019.04.042.

13. *Electrolyte materials for protonic ceramic electrochemical cells: Main limitations and potential solutions.* **Anna V. Kasyanova, Inna A. Zvonareva, Natalia A. Tarasova, Lei Bi, Dmitry A. Medvedev, Zongping Shao.** Issue 4, s.l. : Materials Reports: Energy, 2022, Vol. Volume 2. https://doi.org/10.1016/j.matre.2022.100158.

14. *Technological challenges in the application of proton conducting ceramics.* **H., Iwahara.** 289-298, s.l. : Solid State Ionics, 1995, Vol. Volume 77. https://doi.org/10.1016/0167-2738(95)00051-7.

15. *Review: recent progress in low-temperature proton-conducting ceramics.* **Yuqing Meng, Jun Gao, Zeyu Zhao, Jake Amoroso, Jianhua Tong, and Kyle S. Brinkman.** pages 9291–9312, s.l. : Journal of Material Science, 2019, Vol. Volume 54. https://doi.org/10.1007/s10853-019-03559-9.

16. *Characterization and testing of glass-ceramic sealants for protonic ceramic electrolysis cells applications.* **S. Anelli, A. Baggio, D. Ferrero, D. Schmider, J. Dailly, M. Santarelli, F. Smeacetto.** Issue 10, s.l. : Ceramics International, 2024, Vols. Volume 50,. https://doi.org/10.1016/j.ceramint.2024.02.240.

17. *Recent progress of perovskite-based electrolyte materials for solid oxide fuel cells and performance optimizing strategies for energy storage applications.* **Muhammad Bilal Hanif, Sajid Rauf, Martin Motola, Zaheer Ud Din Babar, Chang-Jiu Li, Cheng-Xin Li.** s.l. : Materials Research Bulletin, 2022, Vol. Volume146. https://doi.org/10.1016/j.materresbull.2021.111612.

18. ***Tahir, Nur Nadhihah Mohd, Nurul Akidah Baharuddin, Nafisah Osman, Nafisah Osman, and.*** *s.l. : Journal of Alloys and Compounds, 2022. doi: 10.1016/j.jallcom.2021.162458..*

19. Trends in Research and Development of Protonic Ceramic Electrolysis . ***Medvedev, Dmitry.*** *s.l. : International Journal of Hydrogen Energy , 2019. doi: 10.1016/j.ijhydene.2019.08.130..*

20. Proton conducting oxides: A review of materials and applications for renewable energy conversion and storage. ***J. Kim, S. Sengodan, S. Kim, O. Kwon, Y. Bu, G. Kim.*** *606-618, s.l. : Renewable and Sustainable Energy Reviews, Vol. Volume 109. https://doi.org/10.1016/j.rser.2019.04.042..*

21. Proton-conducting ceramic fuel cells: Scale up and stack integration. ***Long Q. Le, Carolina Herradon Hernandez, Marcos Hernandez Rodriguez, Liangzhu Zhu, Chuancheng Duan, Hanping Ding, Ryan P. O'Hayre, Neal P. Sullivan.*** *s.l. : Journal of Power Sources, 2021, Journal of Power Sources, Vol. Volume 482, p. 2. https://doi.org/10.1016/j.jpowsour.2020.228868..*

22. Ferritic stainless steel interconnects for protonic ceramic electrochemical cell stacks:Oxidation behavior and protective coatings. ***Wang, R., Sun, Z., Choi, J., Basu, S. N., Stevenson, J. W., & Tucker, M. C.*** *s.l. : International Journal of Hydrogen Energy, 2019. https://doi.org/10.1016/j.ijhydene.2019.08.041.*

23. Vat photopolymerization of polymers and polymer composites: Processes and applications. ***Ans Al Rashid, Waqas Ahmed, Muhammad Yasir Khalid, Muammer Koç.*** *s.l. : Additive Manufacturing, 2021, Vol. Volume 47. https://doi.org/10.1016/j.addma.2021.102279..*

24. Dispersion of Nano-Sized γ-Alumina Powder in Non-Polar Solvents. ***Jen-Chieh Liu, Jau-Ho Jean,Chia-Chen Li.*** *s.l. : Journal of the American Ceramic Society , 2006. https://doi.org/10.1111/j.1551-2916.2005.00858.x.*

25. The role of plasticizer in optimizing the rheological behavior of ceramic pastes intended for stereolithography-based additive manufacturing. ***Jianbin Nie, Maoshan Li, Weiwei Liu, Wenli Li, Zhanwen Xing.*** *Issue 1, s.l. : Journal of the European Ceramic Society, 2021, Vols. Volume 41,. https://doi.org/10.1016/j.jeurceramsoc.2020.08.013.*

26. ***Barnes, Howard A.*** *A HANDBOOK OF ELEMENTARY RHEOLOGY. s.l. : The University of Wales Institute of Non-Newtonian Fluid, 2000. ISBN 0-9538032-0-1.*

27. Selection strategy of curing depth for vat photopolymerization 3D printing of Al2O3 ceramics. ***Xiang Li, Haijun Su, Dong Dong, Hao Jiang, Yuan Liu, Zhonglin Shen, Yinuo Guo, Zhuo Zhang,***

Min Guo. *s.l. : Additive Manufacturing, 2024, Vol. Volume 88. https://doi.org/10.1016/j.addma.2024.104240.*

28. Recent innovations in interfacial strategies for DLP 3D printing process optimization. ***Lei Wu, Yanlin Song.*** *s.l. : Journal Article, 2025. doi:10.1039/d4mh01160k.*

29. The effect of light scattering in stereolithography ceramic manufacturing. ***Chuchu Qian, Kehui Hu, Junhua Li, Peijie Li, Zhigang Lu.*** *Issue 14, s.l. : Journal of the European Ceramic Society, 2021, Vol. Volume 41. https://doi.org/10.1016/j.jeurceramsoc.2021.07.017.*

30. ***Media, CreaTech.*** *Heating Microscope EM301 - Thermo-Optical Analysis. [Online] https://www.hesse-instruments.de/en/products/em301-heating-microscope/.*

31. ***Anelli, Simone.*** *Advanced strategies for Solid Oxide . 2020.*

32. ***Tom, Justin.*** *UV-Vis Spectroscopy: Principle, Strengths and Limitations and Applications. s.l. : Technology Networks, 2023.*

33. Discovery and Understanding of the Ambient-Condition Degradation of Doped Barium Cerate Proton-Conducting Perovskite Oxide in Solid Oxide Fuel Cells. ***Luo, X. Meng, B., Zhao, M. , Xie, H. , Bian, L. , Yang, X..*** *162, s.l. : Journal of The Electrochemical Society, 2015. 162. F1408-F1414. 10.1149/2.0371514jes.*

34. Effect of monomers with different functionalities on stability, rheology, and curing behavior of ceramic suspensions,. ***Lifu Lin, Haidong Wu,Zhaoquan Huang, Shanghua Wu.*** *s.l. : Materials Chemistry and Physics, 2022, Vol. Volume 275. https://doi.org/10.1016/j.matchemphys.2021.125243.*

35. A comprehensive review of the photopolymerization of ceramic resins used in stereolithography. ***Setareh Zakeri, Minnamari Vippola, Erkki Levänen.*** *s.l. : Additive Manufacturing, 2020, Vol. Volume 35. https://doi.org/10.1016/j.addma.2020.101177.*

36. Development of a high solid loading β-TCP suspension with a low refractive index contrast for DLP -based ceramic stereolithography. ***Xiaolong Huang, Honglian Dai, Yafeng Hu, Pengzhen Zhuang, Zhiliang Shi, Yule Ma.*** *Issue 6, s.l. : Journal of the European Ceramic Society, 2021, Vol. Volume 41. https://doi.org/10.1016/j.jeurceramsoc.2020.12.047.*

37. Photopolymerization of Ceramic Resins by Stereolithography. ***Alessandro Bove, Flaviana Calignano ,Manuela Galati,Luca Iuliano.*** *s.l. : Applied Sciences, 2022. https://doi.org/10.3390/app12073591.*

38. Sintering aids for proton-conducting oxides– A double-edged sword?A mini review. ***Ji Lia, Chao Wangb, Xianfen Wangc, Lei Bi.*** *s.l. : Electrochemistry Communications, 2019. https://doi.org/10.1016/j.elecom.2020.106672.*

39. Ferritic Stainless Steel Interconnects for Protonic Ceramic Electrochemical Cell Stacks. ***Wang, Ruofan.*** *2019, Elsevier, p. 4.*

40. ***United nations.*** *UNEP Emissions Gap Report 2024. 2024.*